

# Thermoplasticity and strain localization in transversely isotropic materials based on anisotropic critical state plasticity

Shabnam J. Semnani<sup>1</sup>, Joshua A. White<sup>2</sup> and Ronaldo I. Borja<sup>1,\*</sup>,<sup>†</sup>

<sup>1</sup> *Department of Civil and Environmental Engineering, Stanford University, Stanford, CA 94305, U.S.A.*

<sup>2</sup> *Atmospheric, Earth, and Energy Division, Lawrence Livermore National Laboratory, Livermore, CA 94550, U.S.A.*

## SUMMARY

Geomaterials such as soils and rocks are inherently anisotropic and sensitive to temperature changes caused by various internal and external processes. They are also susceptible to strain localization in the form of shear bands when subjected to critical loads. We present a thermoplastic framework for modeling coupled thermomechanical response and for predicting the inception of a shear band in a transversely isotropic material using the general framework of critical state plasticity and the specific framework of an anisotropic modified Cam–Clay model. The formulation incorporates anisotropy in both elastic and plastic responses under the assumption of infinitesimal deformation. The model is first calibrated using experimental data from triaxial tests to demonstrate its capability in capturing anisotropy in the mechanical response. Subsequently, stress-point simulations of strain localization are carried out under two different conditions, namely, isothermal localization and adiabatic localization. The adiabatic formulation investigates the effect of temperature on localization via thermomechanical coupling. Numerical simulations are presented to demonstrate the important role of anisotropy, hardening, and thermal softening on strain localization inception and orientation. Copyright © 2016 John Wiley & Sons, Ltd.

Received 19 January 2016; Revised 4 April 2016; Accepted 5 April 2016

KEY WORDS: anisotropy; bifurcation; shear band; thermoplasticity; transverse isotropy

## 1. INTRODUCTION

Geomaterials such as soils and rocks are inherently anisotropic, sensitive to changes in temperature, and prone to strain localization. A common form of localized deformation is a deformation band, a tabular zone of intense deformation that includes shear bands, dilation bands, compaction bands, and mixed-mode bands [1, 2]. Strain localization is generally considered as a manifestation of material instability and has been linked traditionally to failure of materials. There has been significant progress in the development of localization theory in the context of shear bands [3–10]; however, a majority of the literature has focused on isothermal localization on isotropic materials. Work involving non-isothermal shear band localization on anisotropic materials remains scarce.

Geomaterials are sensitive to temperature changes that could be significant in many engineering applications. For example, temperature changes could impact caprock integrity in the thermal stimulation of heavy oil reservoirs [11] or during injection of supercritical CO<sub>2</sub> during geologic carbon sequestration [12, 13]. They could also impact activities such as radioactive waste disposal, wellbore drilling, and geothermal and heat storage applications [14–17]. Laboratory investigations reveal that temperature changes influence the mechanical behavior of Tournemire shales [18], clay-rich shales [19], and clayey soils [20]. Various thermoplasticity models have thus been developed

\*Correspondence to: R. I. Borja, Department of Civil and Environmental Engineering, Stanford University, Stanford, CA 94305, U.S.A.

<sup>†</sup>E-mail: borja@stanford.edu

for geomaterials [21–26]. Many of these models focus on the mechanical behavior of shales and/or clays and are based on isotropic critical state plasticity [24, 27–31]. Theoretical developments of coupled thermoplasticity have been reported in [32, 33]; numerical implementations have been reported in [33, 34]; and uniqueness of solution has been reported in [30, 35–37].

Thermal effects manifest themselves in different forms. They could lead to thermal softening, changes in fluid pressure, volume changes, and changes in the material properties. The latter could lead to increased plastic deformation and early onset of material instability. Temperature changes could stem from external heat sources, or they could result from dissipation of energy during high-rate deformation. When thermal conductivity of the material is low and/or when the strain rate is sufficiently high, the heat produced stays local and may lead to softening and, eventually, strain localization. This is generally studied as adiabatic localization in the literature and has been observed in metals, granular materials, ceramics, and polymers [38].

Thermal effects on strain localization were first studied in metals, where significant heat has been observed to be produced within shear bands deforming at high strain rates [39, 40]. Hartley *et al.* [39] showed that small increases in local temperature could enhance localized deformations and lead to the inception of adiabatic shear bands. In geologic formations, shear zones or ductile faults occur by plastic instability involving a softening process, which includes a local increase in temperature caused by shear deformation [41–43]. In tectonics, rapid slip of a rock layer during an earthquake could inhibit fluid flow, as well as prevent the transfer of heat generated from frictional work [44].

Early studies of adiabatic shear bands were restricted to one-dimensional simple shear problems [45–49]. Subsequently, a number of researchers formulated the problem of adiabatic shear bands in a more general setting [50–55]. Duszek and Perzyna [51] presented coupled thermomechanical formulations (using  $J_2$  flow theory) and derived criteria for the inception of adiabatic shear bands in the finite deformation range based on the standard bifurcation theory [7, 8]. They concluded that thermal plastic softening causes the material to become more susceptible to instability in the sense that small increases in temperature during an adiabatic process enhance strain localization. They also showed that, in the context of associative plasticity, strain localization occurs even if the adiabatic critical plastic modulus is positive, whereas it must be negative for isothermal localization. Subsequently, they extended their work to incorporate the effect of damage [52], as well as strain-induced anisotropy and plastic spin [53].

Following the approach in [51], Perzyna [54] introduced a viscoplastic regularization procedure of thermoplastic flow in damaged solids. Runesson *et al.* [55] introduced a regularized strong discontinuity approach in which they first derived an expression for adiabatic thermoplastic tangent stiffness for  $J_2$  plasticity, and then developed closed-form expressions for the critical orientation of the band as well as the critical hardening modulus at plane stress to demonstrate the effect of thermal softening and thermal expansion coefficient. Benallal and Bigoni [50] included thermal effects and thermomechanical coupling into the classical bifurcation analysis [7, 8]. Their formulation assumes that strain, heat flux, and temperature are continuous functions of space, but jumps are allowed in their time derivatives on the localization band.

A number of researchers have studied strain localization within the framework of the finite element method [56–60]. Among them, Ngo *et al.* [59] presented a thermoplastic model for localized failure and the Embedded Discontinuity-Finite Element Method (ED-FEM). In a two-part paper, Armero and Park [56, 57] studied strain localization in one-dimensional shear model under thermally coupled dynamic conditions and discussed the ill-posedness of the problem with regard to the finite element implementation.

In addition to thermal effects, anisotropy plays an important role in the mechanical behavior of geomaterials, as evidenced by laboratory observations on different soils/rocks including Tournemire shale [18], Woodford shale [61], clay-rich shales [19], sedimentary rocks [62], schists [63], and granite rocks [64]. In particular, sedimentary rocks such as shale, sandstone, and claystone demonstrate strong transversely isotropic behavior because of the existence of distinct bedding planes. The majority of plasticity models developed for anisotropic materials are based on extension of isotropic material models. Development of mathematical plasticity models based on an anisotropic yield criterion goes back to the work by Hill [65, 66], who generalized the von Mises yield criterion for orthotropic ductile materials (e.g., metals) by introducing six material parameters that scale

the second-order stress terms appearing in von Mises yield criterion. Subsequently, Hill's model was enhanced by several other researchers [67–69]. Hoffman [68] extended Hill's model by adding three linear stress terms to account for Bauschinger effect, resulting in a model with nine material parameters. Tsai and Wu [70] proposed a more general form of the yield surface represented by the summation of linear and second-order stress terms.

There are three general continuum-based approaches for incorporating anisotropy into the elastoplastic behavior of geomaterials. The first approach follows the lines of Hill [65] and Hoffman [68] as described in the previous paragraph, which have been used in [71, 72] for obtaining failure criteria appropriate for geomaterials. Among them, Parisseau [71] extended the anisotropic failure criterion proposed by Hill [65] for cohesive frictionless materials to cohesive frictional materials by introducing a linear term of three normal stresses in Hill's criterion to describe the pressure dependency.

The second approach employs the idea of a fourth-order projection tensor to incorporate anisotropy [73–76]. Among them, Nova [76] extended the Cam–Clay model to obtain a failure criterion for transversely isotropic soft sedimentary rocks in triaxial compression by using a fourth-order tensor to rotate the equation for the yield function around the hydrostatic axis. Cazacu *et al.* [74] and Cazacu and Cristescu [77] used the same idea to extend the so-called Mises–Schleicher criterion for isotropic material to transversely isotropic material. Crook *et al.* [75] extended the modified Cam–Clay (MCC) model by choosing the components of the fourth-order tensor to be the same as those in the model of Hashagen and de Borst [67] using the Hoffman criterion [68].

The third approach uses the notion of microstructural tensor to obtain failure criteria for anisotropic materials [78–82]. Pietruszczak and Mroz [82] and Pietruszczak *et al.* [81] presented a formulation that incorporates microstructure using a second-order tensor whose eigenvectors specify the orientation of the axes of material symmetry. They formulated their failure criterion in terms of the stress state and a microstructure tensor. Chen *et al.* [79] extended the model developed by Pietruszczak *et al.* [81] to incorporate induced damage. They coupled plastic deformations with damage produced by microcrack growth and used triaxial test results on Tournemire shale to validate their model.

A majority of the aforementioned formulations, however, have focused on one aspect or the other but have not investigated the combined effects of inherent anisotropy and temperature on strain localization. In this paper, we derive a transversely isotropic plasticity model from the well-known MCC model under the assumption of infinitesimal deformation. We show that one can obtain the same result employing either a fourth-order projection tensor or a second-order microstructure tensor perspective. We also develop the coupled thermoplastic constitutive equations and obtain isothermal as well as adiabatic relations for the proposed anisotropic model. Subsequently, we calibrate the model using experimental data on Tournemire shale from Niandou *et al.* [83] to demonstrate its capability in capturing anisotropic mechanical responses. Finally, we conduct stress-point simulations under plane strain conditions to investigate strain localization under (i) isothermal condition and (ii) adiabatic condition. We note that adiabatic localization allows for jumps in the temperature field in addition to jumps in the velocity field typically encountered in isothermal localization [84]. Numerical simulations are presented to demonstrate the influence of anisotropy, hardening, and thermal softening on strain localization.

## 2. MOTIVATIONS FROM THERMODYNAMICS

We recall the first law of thermodynamics (balance of energy),

$$\dot{e} = \boldsymbol{\sigma} : \boldsymbol{\epsilon} - \text{div}(\mathbf{q}) + r_t, \quad (1)$$

and the second law (Clausius–Duhem inequality),

$$\mathcal{D}_{int} = \dot{\eta} + \text{div}\left(\frac{\mathbf{q}}{\Theta}\right) - \frac{r_t}{\Theta} \geq 0, \quad (2)$$

where  $\dot{\square}$  denotes a derivative with respect to time,  $e$  is internal energy per unit volume,  $\mathbf{q}$  is the heat flux vector,  $\Theta$  is absolute temperature,  $\boldsymbol{\sigma}$  is the symmetric Cauchy stress tensor,  $\boldsymbol{\epsilon}$  is the infinitesimal

total strain tensor, and  $r_t$  denotes a heat source. The expression for the internal energy dissipation  $\mathcal{D}_{int}$  contains an entropy term  $\eta$  that is related to Helmholtz free energy  $\Psi$  as

$$\Psi = e - \Theta \eta. \quad (3)$$

The heat flux vector  $\mathbf{q}$  can be obtained using Duhamel–Fourier’s law for heat conduction, which takes the form

$$\mathbf{q} = -\boldsymbol{\kappa} \cdot \nabla \Theta, \quad (4)$$

where  $\boldsymbol{\kappa}$  is the thermal conductivity tensor. Combining Equations (1)–(3) leads to the dissipation inequality of the form

$$\mathcal{D}_{int} = \boldsymbol{\sigma} : \dot{\boldsymbol{\epsilon}} - (\eta \dot{\Theta} + \dot{\Psi}) - \frac{1}{\Theta} \mathbf{q} \cdot \nabla \Theta \geq 0, \quad (5)$$

and balance of energy of the form

$$\dot{\Psi} + \dot{\eta} \Theta + \eta \dot{\Theta} + \text{div}(\mathbf{q}) - \boldsymbol{\sigma} : \boldsymbol{\epsilon} - r_t = 0. \quad (6)$$

We consider a Helmholtz free energy function for thermoelastoplastic anisotropic materials of the form

$$\Psi = \hat{\Psi}(\boldsymbol{\epsilon}, \Theta, \boldsymbol{\xi}), \quad (7)$$

where  $\boldsymbol{\xi}$  is a vector of plastic internal state variables describing dissipation occurring during thermoplastic flow. Using Equation (3), the dissipation inequality reduces to the form

$$\left( \boldsymbol{\sigma} - \frac{\partial \Psi}{\partial \boldsymbol{\epsilon}} \right) : \dot{\boldsymbol{\epsilon}} + \left( \frac{\partial \Psi}{\partial \Theta} + \eta \right) \dot{\Theta} - \frac{\partial \Psi}{\partial \boldsymbol{\xi}} \dot{\boldsymbol{\xi}} - \frac{1}{\Theta} \mathbf{q} \cdot \nabla \Theta \geq 0. \quad (8)$$

Standard Coleman–Noll arguments lead to the constitutive relations

$$\boldsymbol{\sigma} = \frac{\partial \Psi}{\partial \boldsymbol{\epsilon}}, \quad \eta = -\frac{\partial \Psi}{\partial \Theta}, \quad (9)$$

and

$$-\frac{\partial \Psi}{\partial \boldsymbol{\xi}} \dot{\boldsymbol{\xi}} - \frac{1}{\Theta} \mathbf{q} \cdot \nabla \Theta \geq 0. \quad (10)$$

Substituting the entropy rate into Equation (6) gives

$$\rho c \dot{\Theta} = \Theta \frac{\partial^2 \Psi}{\partial \boldsymbol{\epsilon} \partial \Theta} : \dot{\boldsymbol{\epsilon}} + \left( \Theta \frac{\partial^2 \Psi}{\partial \boldsymbol{\xi} \partial \Theta} - \frac{\partial \Psi}{\partial \boldsymbol{\xi}} \right) \dot{\boldsymbol{\xi}} - \text{div}(\mathbf{q}) + r_t, \quad (11)$$

in which  $\rho$  denotes mass density and  $c$  is heat capacity (per unit mass) defined such that

$$\rho c = -\Theta \frac{\partial^2 \Psi}{\partial \Theta \partial \Theta}. \quad (12)$$

Following an approach similar to the one presented by Duszek and Perzyna [51] for large deformation and  $J_2$  plasticity, we define a complementary energy function as

$$\Omega = \hat{\Omega}(\boldsymbol{\sigma}, \Theta, \boldsymbol{\xi}) = \boldsymbol{\sigma} : \boldsymbol{\epsilon} - \hat{\Psi}(\boldsymbol{\epsilon}, \Theta, \boldsymbol{\xi}), \quad (13)$$

which gives

$$\frac{\partial \Omega}{\partial \boldsymbol{\sigma}} = \boldsymbol{\epsilon}. \quad (14)$$

Thus, the total strain rate can be obtained as

$$\dot{\boldsymbol{\epsilon}} = \underbrace{\frac{\partial^2 \Omega}{\partial \boldsymbol{\sigma} \partial \boldsymbol{\sigma}} : \dot{\boldsymbol{\sigma}}}_{\dot{\boldsymbol{\epsilon}}^e} + \underbrace{\frac{\partial^2 \Omega}{\partial \boldsymbol{\sigma} \partial \Theta} \dot{\Theta}}_{\dot{\boldsymbol{\epsilon}}^t} + \underbrace{\frac{\partial^2 \Omega}{\partial \boldsymbol{\sigma} \partial \boldsymbol{\xi}} \cdot \dot{\boldsymbol{\xi}}}_{\dot{\boldsymbol{\epsilon}}^p} = \mathbb{S} : \dot{\boldsymbol{\sigma}} - \boldsymbol{\alpha}^t \dot{\Theta} + \boldsymbol{\Xi} \cdot \dot{\boldsymbol{\xi}} \quad (15)$$

Equation (15) shows decomposition of the total strain rate into three components, namely, an elastic strain rate  $\dot{\epsilon}^e$ , a thermal strain rate  $\dot{\epsilon}^t$ , and a plastic strain rate  $\dot{\epsilon}^p$ . The fourth-order tensor  $\mathbb{S} = \partial^2 \Omega / \partial \sigma \partial \sigma$  is an elastic compliance tensor, whereas  $\alpha^t = -\partial^2 \Omega / \partial \sigma \partial \Theta$  is a second-order tensor containing thermal expansion coefficients. We can also obtain the rate of change of  $\sigma$  from Equation (9) while holding the plastic internal state vector constant, which gives

$$\dot{\sigma} = \frac{\partial^2 \Psi}{\partial \epsilon \partial \epsilon} : \dot{\epsilon}^e + \frac{\partial^2 \Psi}{\partial \Theta \partial \epsilon} \dot{\Theta}, \tag{16}$$

where  $\partial^2 \Psi / \partial \epsilon \partial \epsilon = \mathbb{C}^e = \mathbb{S}^{-1}$  is the elastic stiffness tangential tensor. Appendix A defines the components of the elastic tangent tensor for a transversely isotropic linear elastic material.

Consider a plastic potential function  $g = \hat{g}(\sigma, \kappa, \Theta)$  that determines the direction of the plastic strain rate through the relation

$$\dot{\epsilon}^p = \dot{\lambda} \frac{\partial g}{\partial \sigma}, \tag{17}$$

where  $\dot{\lambda} \geq 0$  is the plastic consistency parameter, and  $\kappa$  represents the hardening parameter. Comparing (15) and (17) gives

$$\dot{\xi} = \dot{\lambda} \Xi^{-1} : \frac{\partial g}{\partial \sigma}. \tag{18}$$

Upon substitution of (18) into the balance of energy Equation (11), we obtain

$$\rho c \dot{\Theta} = \Theta \frac{\partial \sigma}{\partial \Theta} : \dot{\epsilon} + \Theta \left( \frac{\partial^2 \Psi}{\partial \xi \partial \Theta} \cdot \Xi^{-1} \right) : \dot{\epsilon}^p - \frac{\partial \Psi}{\partial \xi} \cdot \Xi^{-1} : \dot{\epsilon}^p - \text{div}(\mathbf{q}) + r_t. \tag{19}$$

This implies that for the thermoelastoplastic solid considered in this paper, the thermal contributions originate from two different processes, namely, external heat source and internal mechanical work. The main contribution to the internal mechanical work comes from plastic deformation [51]. Thus, Equation (19) can be rewritten as

$$\rho c \dot{\Theta} = \zeta \sigma : \dot{\epsilon}^p - \text{div}(\mathbf{q}) + r_t, \tag{20}$$

where  $\zeta$  is determined from the equation

$$\zeta \frac{\partial \Psi}{\partial \epsilon} = \left( \frac{\partial^2 \Psi}{\partial \xi \partial \Theta} - \frac{\partial \Psi}{\partial \xi} \right) \cdot \Xi^{-1}. \tag{21}$$

It is worth noting that very often in the literature the internal contribution to temperature rate is determined from a similar equation of the form  $\rho \sigma : \dot{\epsilon}^p$ , where  $\rho$  is the Taylor–Quinney coefficient [45, 47, 56–58, 85] describing the portion of plastic work converted into heat. The parameter  $\zeta$  defined in this paper is conceptually analogous to the Taylor–Quinney coefficient. Equation (20) is used later in this paper to introduce thermomechanical coupling into the constitutive formulation.

### 3. CONSTITUTIVE THEORY

This section proposes a constitutive theory for anisotropic materials, using the notion of a fictitious isotropic configuration. This is facilitated by defining a microstructure tensor and a projection operator that maps the real Cauchy stress tensor  $\sigma$  to an alternative stress configuration  $\sigma^*$  whose behavior may be computed using standard isotropic models.

### 3.1. Mathematical representation of anisotropy

Consider a projection operator  $\mathbb{P}$  mapping the real Cauchy stress tensor  $\boldsymbol{\sigma}$  to an alternative stress configuration  $\boldsymbol{\sigma}^*$ ,

$$\boldsymbol{\sigma}^* = \mathbb{P} : \boldsymbol{\sigma} \quad (22)$$

where  $\mathbb{P}$  is a fourth-order tensor possessing both major and minor symmetry. The anisotropic yield function in the real stress configuration is assumed to be equivalent to an isotropic yield function in the projected configuration as follows:

$$f(\boldsymbol{\sigma}) = f_{iso}(\boldsymbol{\sigma}^*) . \quad (23)$$

This conveniently allows one to extend a standard isotropic plasticity model into the anisotropic regime through the definition of an appropriate stress projection.

To define the projection operation, let  $\boldsymbol{l}_1$ ,  $\boldsymbol{l}_2$ , and  $\boldsymbol{l}_3$  be three mutually orthogonal unit vectors in the direction of axes 1, 2, and 3, respectively, as shown in Figure 1. The material is isotropic in the 2–3 plane. For this configuration, the material symmetry group  $\mathcal{G}$  is defined as

$$\mathcal{G} = \{\boldsymbol{Q} \mid \boldsymbol{Q} \cdot \boldsymbol{l}_1 = \boldsymbol{l}_1\}, \quad (24)$$

where  $\boldsymbol{Q}$  is a proper orthogonal rotation—with properties  $\boldsymbol{Q}^T = \boldsymbol{Q}^{-1}$  and  $\det(\boldsymbol{Q}) = 1$ . That is,  $\boldsymbol{l}_1$  is an eigenvector of any rotation  $\boldsymbol{Q} \in \mathcal{G}$  preserving material symmetry. Now let

$$\boldsymbol{\phi} = \boldsymbol{l}_1 \otimes \boldsymbol{l}_1 \quad (25)$$

denote a second-order microstructure tensor describing the bedding orientation. This tensor possesses the important property

$$\boldsymbol{Q} \cdot \boldsymbol{\phi} \cdot \boldsymbol{Q}^T = \boldsymbol{\phi} \quad \forall \boldsymbol{Q} \in \mathcal{G}. \quad (26)$$

Using this microstructure tensor, we define the following relationship between the real and effective stress states,

$$\boldsymbol{\sigma}^* = c_1 \boldsymbol{\sigma} + c_2 (\boldsymbol{\phi} \cdot \boldsymbol{\sigma} \cdot \boldsymbol{\phi}) + \frac{c_3}{2} (\boldsymbol{\sigma} \cdot \boldsymbol{\phi} + \boldsymbol{\phi} \cdot \boldsymbol{\sigma}), \quad (27)$$

where  $c_1$ ,  $c_2$ ,  $c_3$  are three material coefficients. This operation can be recast in the form (22) by defining a fourth-order projection tensor  $\mathbb{P}$  with components

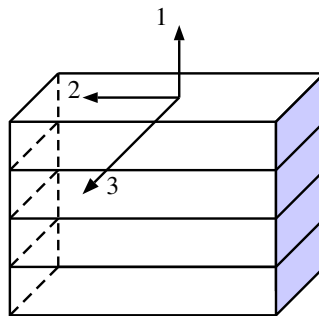


Figure 1. Schematic of orthogonal basis for transversely isotropic material. Axis 1 is the axis of symmetry, whereas axes 2 and 3 define the plane of isotropy.

$$\begin{aligned} \mathbb{P}_{ijkl} = & \frac{c_1}{2} (\delta_{ik}\delta_{jl} + \delta_{il}\delta_{jk}) \\ & + \frac{c_2}{2} (\phi_{ik}\phi_{jl} + \phi_{il}\phi_{jk}) \\ & + \frac{c_3}{4} (\delta_{ik}\phi_{jl} + \delta_{il}\phi_{jk} + \phi_{ik}\delta_{jl} + \phi_{il}\delta_{jk}). \end{aligned} \tag{28}$$

When the coordinate system is aligned with the bedding planes, this projection operation has a particularly simple structure. In matrix notation,

$$\begin{pmatrix} \sigma_{11}^* \\ \sigma_{22}^* \\ \sigma_{33}^* \\ \sigma_{23}^* \\ \sigma_{13}^* \\ \sigma_{12}^* \end{pmatrix} = \begin{bmatrix} \alpha & & & & & \\ & \beta & & & & \\ & & \beta & & & \\ & & & \beta & & \\ & & & & \gamma & \\ & & & & & \gamma \end{bmatrix} \begin{pmatrix} \sigma_{11} \\ \sigma_{22} \\ \sigma_{33} \\ \sigma_{23} \\ \sigma_{13} \\ \sigma_{12} \end{pmatrix}, \tag{29}$$

where the entries of the projection matrix are  $\alpha = (c_1 + c_2 + c_3)$ ,  $\beta = c_1$ , and  $\gamma = (c_1 + c_3/2)$ . One observes that the stress components are simply scaled by a diagonal matrix whose coefficients are chosen to preserve material symmetry requirements.

Now, consider the decomposition of the Cauchy stress tensor into volumetric and deviatoric parts,

$$\boldsymbol{\sigma} = p\mathbf{1} + \mathbf{s}, \tag{30}$$

in which  $p = \text{tr}(\boldsymbol{\sigma})/3$  is the mean normal stress,  $\mathbf{1}$  is the second-rank identity tensor, and  $\mathbf{s}$  is the deviatoric stress. Let  $q = \sqrt{3/2}\|\mathbf{s}\|$ . The stress invariants  $p$  and  $q$  provide a convenient basis for defining an objective yield function in the isotropic setting. In particular, the isotropic MCC yield function takes the form

$$f_{iso}(\boldsymbol{\sigma}) = \frac{q^2}{M^2} + p(p - p_c) \leq 0, \tag{31}$$

where  $M$  is the slope of the critical state line and  $p_c$  is the preconsolidation pressure, a state variable controlling the size of the yield surface. Introducing the operators

$$\mathbb{D} = \frac{1}{3}\mathbb{A} = \mathbb{I} - \frac{1}{3}\mathbf{1} \otimes \mathbf{1}, \quad \mathbf{a} = \frac{1}{3}\mathbf{1}, \tag{32}$$

where  $\mathbb{I}$  is the fourth-rank symmetric identity tensor with components  $I_{ijkl} = (\delta_{ik}\delta_{jl} + \delta_{il}\delta_{jk})/2$ , it is easy to show (by expansion, for example) that

$$p = \mathbf{a} : \boldsymbol{\sigma} \tag{33}$$

and

$$q = \sqrt{\frac{3}{2}} \|\mathbb{D} : \boldsymbol{\sigma}\| = \sqrt{\frac{1}{2}} \|\boldsymbol{\sigma}\|_{\mathbb{A}}, \tag{34}$$

where  $\|\cdot\|_{\square}$  denotes a norm in the metric  $\square$  such that  $\|\boldsymbol{\sigma}\|_{\mathbb{A}} = \sqrt{\boldsymbol{\sigma} : \mathbb{A} : \boldsymbol{\sigma}}$  and  $\|\cdot\| = \|\cdot\|_{\mathbb{I}}$ . More explicitly,

$$f_{iso}(\boldsymbol{\sigma}) = \frac{\|\boldsymbol{\sigma}\|_{\mathbb{A}}^2}{2M^2} + (\mathbf{a} : \boldsymbol{\sigma})(\mathbf{a} : \boldsymbol{\sigma} - p_c) \leq 0 \tag{35}$$

defines the yield function for an isotropic two-invariant MCC model.

Now, consider once again the projection operator  $\mathbb{P}$  and define

$$\mathbb{A}^* = \mathbb{P} : \mathbb{A} : \mathbb{P}, \quad \mathbf{a}^* = \mathbb{P} : \mathbf{a}. \tag{36}$$

The invariants  $p$  and  $q$  can be transformed accordingly as

$$p^* = \mathbf{a}^* : \boldsymbol{\sigma} \tag{37}$$

and

$$q^* = \sqrt{\frac{1}{2}} \|\boldsymbol{\sigma}\|_{\mathbb{A}^*} . \tag{38}$$

Note that  $p^*$  and  $q^*$  are now mixed invariants of the stress  $\boldsymbol{\sigma}$  and microstructure tensor  $\boldsymbol{\phi}$ . The yield function for a transversely isotropic material can now be written in terms of these modified invariants as

$$f(\boldsymbol{\sigma}) = \frac{q^{*2}}{M^2} + p^*(p^* - p_c) \leq 0, \tag{39}$$

or, more explicitly,

$$f(\boldsymbol{\sigma}) = \frac{\|\boldsymbol{\sigma}\|_{\mathbb{A}^*}^2}{2M^2} + (\mathbf{a}^* : \boldsymbol{\sigma})(\mathbf{a}^* : \boldsymbol{\sigma} - p_c) \leq 0. \tag{40}$$

If  $\alpha = \beta = \gamma = 1$ , the anisotropic formulation reduces to the special case of an isotropic material. Figure 2 shows schematics of the transversely isotropic yield function in  $p^*$ - $q^*$  and  $p$ - $q$  spaces for different values of  $\alpha$  and  $\beta$ . Matrix representation of Equation (40) can be written as follows, which will be used later in this paper for greater clarity in representation of the local tangent operator.

$$f = \frac{1}{2M^2} (\bar{\boldsymbol{\sigma}}^T \cdot [\mathbf{A}_T] \cdot \bar{\boldsymbol{\sigma}}) + (\bar{\mathbf{a}}_T \bar{\boldsymbol{\sigma}})(\bar{\mathbf{a}}_T \bar{\boldsymbol{\sigma}} - p_c) \leq 0, \tag{41}$$

where  $\bar{\boldsymbol{\sigma}} = [\sigma_{11} \ \sigma_{22} \ \sigma_{33} \ \sigma_{23} \ \sigma_{13} \ \sigma_{12}]^T$  and

$$[\mathbf{A}_T] = \begin{bmatrix} 2\alpha^2 & -\alpha\beta & -\alpha\beta & 0 & 0 & 0 \\ -\alpha\beta & 2\beta^2 & -\beta^2 & 0 & 0 & 0 \\ -\alpha\beta & -\beta^2 & 2\beta^2 & 0 & 0 & 0 \\ 0 & 0 & 0 & 6\beta^2 & 0 & 0 \\ 0 & 0 & 0 & 0 & 6\gamma^2 & 0 \\ 0 & 0 & 0 & 0 & 0 & 6\gamma^2 \end{bmatrix} \tag{42}$$

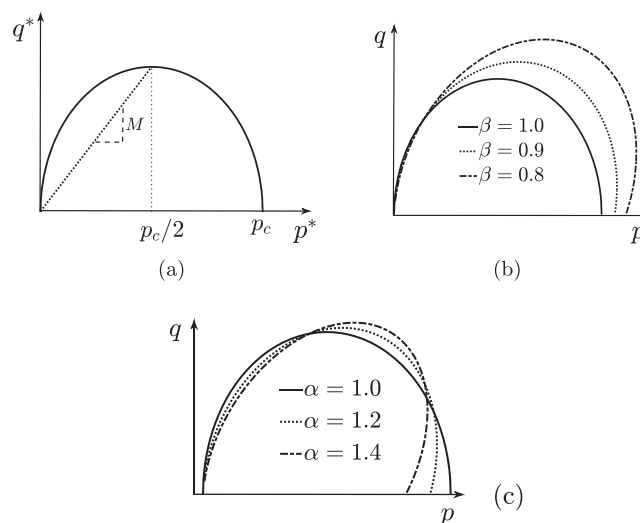


Figure 2. Schematic representation of a transversely isotropic modified Cam–Clay model in (a)  $p^*$ - $q^*$  space; (b)  $p$ - $q$  space for  $\alpha = 1$  and different values of  $\beta$ ; (c)  $p$ - $q$  space for  $\beta = 1$  and different values of  $\alpha$ .

and

$$\bar{\mathbf{a}}_T = [\alpha/3 \ \beta/3 \ \beta/3 \ 0 \ 0 \ 0] . \tag{43}$$

Assuming an associative flow rule, the yield function can be used to obtain the plastic flow direction using Equation (17) and  $g = f$ . We remark that the plastic flow direction is determined by the gradient of the plastic potential function with respect to  $\sigma$  and not with respect to  $\sigma^*$ . In particular,

$$\dot{\epsilon}^p = \dot{\lambda} \frac{\partial f}{\partial \sigma} = \dot{\lambda} \frac{\partial f_{iso}}{\partial \sigma^*} : \frac{\partial \sigma^*}{\partial \sigma} = \dot{\lambda} \mathbb{P} : \frac{\partial f_{iso}}{\partial \sigma^*} . \tag{44}$$

An advantage of the previous representation is that one can simply replace  $\mathbf{a}^*$  with  $\mathbf{a}$  to attribute anisotropy to only the deviatoric component of stress. This induces an isotropic pressure dependence into the model that may be favorable for some types of material such as pressure-sensitive rocks. We employ this strategy in the numerical examples to follow. Note that, however, in this situation, four material parameters appear in the deviatoric term of the yield function – that is,  $\alpha$ ,  $\beta$ ,  $\gamma$ , and  $M$  – but a non-uniqueness issue arises in their selection. In particular, note that  $\mathbb{P}$  and  $M$  may be simultaneously scaled by an arbitrary constant without changing the ratio  $q^{*2}/M^2$ . Thus, an infinite number of parameter combinations may be found that giving the same material response. This situation is easily remedied by fixing one of the material parameters (e.g., fixing  $\gamma = 1$ ) and only using the remaining three for fitting purposes.

While not pursued here, it may be observed that a similar approach can be used to extend the mathematical formulation to even more general conditions, including orthotropic materials, by including additional terms in the definition of the projection operation  $\mathbb{P}$ .

### 3.2. Thermomechanical hardening and softening

The hardening parameter that defines the growth/shrinkage of the yield surface is the preconsolidation pressure  $p_c$ . The evolution of  $p_c$  consists of two parts, a mechanical hardening/softening due to plastic deformation and a thermal hardening/softening. An exponential nonlinear mechanical hardening law is typically adopted in the literature alongside the MCC model. The following general format can be used to represent a thermomechanical hardening law:

$$p_c = p_{c0} \exp\left(\frac{\epsilon_v^p}{\lambda^p}\right) \mathcal{G}(\Theta) + \mathcal{A}(\Theta) , \tag{45}$$

where  $\lambda^p = C_c - C_r$ , with  $C_r > 0$  being the elastic compressibility index and  $C_c > C_r$  being the total compressibility index;  $\epsilon_v^p = \text{tr}(\epsilon^p)$  is the plastic volumetric strain; and  $p_{c0}$  is the preconsolidation pressure at an initial temperature  $\Theta_0$ . Furthermore,  $\mathcal{G}(\Theta)$  and  $\mathcal{A}(\Theta)$  are thermal softening functions. Several representations of these functions have been proposed in the literature, three of which are summarized in the succeeding text.

The Hueckel and Borsetto [29] softening function takes the form

$$\mathcal{G}(\Theta) = \exp(-a_0 \Delta\Theta \epsilon_v^p / \lambda^p) , \quad \mathcal{A}(\Theta) = 2(a_1 \Delta\Theta + a_2 \Delta\Theta^2) , \tag{46}$$

where  $a_0$ ,  $a_1$ , and  $a_2$  are softening material parameters and  $\Delta\Theta = \Theta - \Theta_0$ . The Picard [86] softening law is of the form

$$\mathcal{G}(\Theta) = \exp(-a_0 \Theta) , \quad \mathcal{A}(\Theta) = 0 . \tag{47}$$

Finally, the Laloui and Cekerevac [22] softening law has the form

$$\mathcal{G}(\Theta) = \left[ 1 - \gamma_T \ln\left(1 + \frac{\Delta\Theta}{\Theta_0 - 273}\right) \right] , \quad \mathcal{A}(\Theta) = 0 , \tag{48}$$

where  $\gamma_T$  is another material parameter. In the present formulation, we adopt the model proposed by Laloui and Cekerevac [22]; thus, we can write the hardening law as

$$p_c = p_{c0} \exp\left(\frac{\epsilon_v^p}{\lambda^p}\right) \left[ 1 - \gamma_T \ln\left(1 + \frac{\Delta\Theta}{\Theta_0 - 273}\right) \right] . \tag{49}$$

It should be noted that Laloui and Cekerevac [22] used temperature in Celsius to present and calibrate their model. To comply with their formulation, the denominator in Equation (49) has been modified to reflect the fact that  $\Theta$  is defined as absolute temperature.

### 3.3. Continuum formulation

Considering the yield function presented in Equation (39), the consistency condition requires that

$$\dot{f}(\boldsymbol{\sigma}, p_c(\epsilon_v^p, \Theta)) = \frac{\partial f}{\partial \sigma_{ij}} \dot{\sigma}_{ij} + \frac{\partial f}{\partial p_c} \left[ \frac{\partial p_c}{\partial \epsilon_v^p} \dot{\epsilon}_v^p + \frac{\partial p_c}{\partial \Theta} \dot{\Theta} \right] = 0. \quad (50)$$

Combining Equations (15) and (17), together with the elastic constitutive relation  $\dot{\boldsymbol{\sigma}} = \mathbb{C}^e : \dot{\boldsymbol{\epsilon}}^e$ , we write, in indicial notation,

$$\dot{\sigma}_{ij} = C_{ijkl}^e \left( \dot{\epsilon}_{kl} - \dot{\lambda} \frac{\partial f}{\partial \sigma_{kl}} - \dot{\epsilon}_{kl}^t \right). \quad (51)$$

Substituting (51) and the hardening law given in (49) into the consistency condition (50), we obtain

$$\frac{\partial f}{\partial \sigma_{ij}} C_{ijkl}^e \left( \dot{\epsilon}_{kl} - \dot{\lambda} \frac{\partial f}{\partial \sigma_{kl}} - \dot{\epsilon}_{kl}^t \right) + \frac{\partial f}{\partial p_c} \left[ \text{tr} \left( \frac{\partial f}{\partial \sigma_{ij}} \right) \left( \frac{p_c}{\lambda^p} \right) \dot{\lambda} - \tilde{H}_T \dot{\Theta} \right] = 0, \quad (52)$$

where

$$\tilde{H}_T = \left( \frac{\gamma_T}{\Theta} \right) p_{c0} \exp \left( \frac{\epsilon_v^p}{\lambda^p} \right) \quad (53)$$

and

$$\dot{\epsilon}_v^p = \text{tr} \left( \dot{\lambda} \frac{\partial f}{\partial \boldsymbol{\sigma}} \right) = \dot{\lambda} \text{tr} \left( \frac{\partial f}{\partial \boldsymbol{\sigma}} \right). \quad (54)$$

The plastic flow rate is then derived as

$$\dot{\lambda} = \frac{1}{\chi} \left[ \frac{\partial f}{\partial \sigma_{ij}} C_{ijkl}^e (\dot{\epsilon}_{kl} - \dot{\epsilon}_{kl}^t) - \frac{\partial f}{\partial p_c} \tilde{H}_T \dot{\Theta} \right], \quad (55)$$

where

$$\chi = \frac{\partial f}{\partial \sigma_{ij}} C_{ijkl}^e \frac{\partial f}{\partial \sigma_{kl}} - \frac{\partial f}{\partial p_c} \left( \frac{p_c}{\lambda^p} \right) \text{tr} \left( \frac{\partial f}{\partial \sigma_{ij}} \right). \quad (56)$$

Upon substitution of (55) back into (51), we obtain

$$\dot{\sigma}_{ij} = C_{ijkl}^{ep} \dot{\epsilon}_{kl} + \tau_{ij} \dot{\Theta}, \quad (57)$$

where

$$C_{ijkl}^{ep} = C_{ijkl}^e - C_{ijkl}^p = C_{ijkl}^e - \frac{1}{\chi} C_{ijpq}^e \frac{\partial f}{\partial \sigma_{mn}} C_{mnkl}^e \frac{\partial f}{\partial \sigma_{pq}} \quad (58)$$

and

$$\tau_{ij} = \frac{1}{\chi} C_{ijpq}^e \frac{\partial f}{\partial p_c} \frac{\partial f}{\partial \sigma_{pq}} \tilde{H}_T + C_{ijkl}^{ep} \alpha_{kl}^t, \quad (59)$$

in which  $\alpha_{kl}^t$  ( $k, l = 1, 2, 3$ ) denote components of thermal expansion coefficient tensor  $\boldsymbol{\alpha}^t$  defined in Equation (15).

The previous equations can be summarized in symbolic tensor notation as follows:

$$\dot{\sigma} = \mathbb{C}^{ep} : \dot{\epsilon} + \tau \dot{\Theta}, \tag{60}$$

where

$$\begin{aligned} \mathbb{C}^{ep} &= \mathbb{C}^e - \mathbb{C}^p \\ \mathbb{C}^p &= \frac{1}{\chi} \left( \mathbb{C}^e : \frac{\partial f}{\partial \sigma} \otimes \frac{\partial f}{\partial \sigma} : \mathbb{C}^e \right) \\ \tau &= \mathbb{C}^{ep} : \alpha^t + \tilde{H}_T \frac{\partial f}{\partial p_c} \mathbb{C}^e : \frac{\partial f}{\partial \sigma} \end{aligned} \tag{61}$$

and

$$\chi = \frac{\partial f}{\partial \sigma} : \mathbb{C}^e : \frac{\partial f}{\partial \sigma} - \frac{\partial f}{\partial p_c} \left( \frac{p_c}{\lambda^p} \right) \text{tr} \left( \frac{\partial f}{\partial \sigma} \right). \tag{62}$$

The numerical integration of the aforementioned constitutive theory is described in the next section.

#### 4. STRESS-POINT INTEGRATION

We use an implicit return mapping algorithm for integrating the rate constitutive equation. The premise is that the variables at time  $t_n$  are given, along with strain and temperature increments  $\Delta \epsilon$  and  $\Delta \Theta$ , respectively, and we are required to calculate all variables at time  $t_{n+1}$ . Because of the inherent anisotropy of the material, the stress and strain tensors are generally non-coaxial. Therefore, the return mapping is performed in full strain space. The algorithm is shown in Box 1.

1. Update temperature  $\Theta_{n+1} = \Theta_n + \Delta \Theta$ .
2. Compute thermal strains:  $\Delta \epsilon_{n+1}^t = -\alpha^t \Delta \Theta$
3. Compute predictor strain:  $\epsilon_{n+1}^{e,tr} = \epsilon_n^e + \Delta \epsilon - \Delta \epsilon_{n+1}^t$
4. Compute trial stress vector:  $\sigma_{n+1}^{tr} = \mathbb{C}^e : \epsilon_{n+1}^{e,tr}$
5. Update preconsolidation pressure:  $p_{c,n+1}^{tr} (\Delta \epsilon_{v,n}^p, \Theta_{n+1})$
6. Compute the yield function  $f (\sigma_{n+1}^{tr}, p_{c,n+1}^{tr})$
7. If  $f < 0$ , set  $\sigma_{n+1} = \sigma_{n+1}^{tr}$ ,  $\epsilon_{n+1}^e = \epsilon_{n+1}^{e,tr}$ ,  $p_{c,n+1} = p_{c,n+1}^{tr}$  and exit.
8. Else, iterate to compute  $\sigma_{n+1}$  and  $p_{c,n+1}$ .

**Box 1.** Return mapping algorithm in strain space for the anisotropic thermoplastic model.

Computation of  $\sigma_{n+1}$  and  $p_{c,n+1}$  goes as follows. For  $\mathcal{A}(\Theta) = 0$ , which is the case with either the Picard [86] or the Laloui and Cekerevac [22] softening law, the incremental form of the preconsolidation pressure used in Step 5 of Box 1 is given by

$$p_{c,n+1} = p_{c,n} \exp \left( \frac{\Delta \epsilon_v^p}{\lambda^p} \right) \frac{\mathcal{G}(\Theta_{n+1})}{\mathcal{G}(\Theta_n)}. \tag{63}$$

Step 8, on the other hand, generally requires an iterative procedure as discussed in the next paragraph.

To compute  $\sigma_{n+1}$  and  $p_{c,n+1}$  in Step 8 of Box 1, we need to impose two constraints. The first is the discrete consistency condition,

$$f (\sigma_{n+1}, p_{c,n+1}) = 0. \tag{64}$$

The second is the discrete version of the flow rule,

$$\epsilon_{n+1}^e = \epsilon_{n+1}^{e,tr} - \Delta \lambda \frac{\partial f}{\partial \sigma_{n+1}}. \tag{65}$$

For greater clarity in the presentation of the local tangent operator, we use matrix representation for some of the tensor quantities (see also Appendix A). We define the following vector quantities:

$$\bar{\epsilon}^e = [\epsilon_{11}^e \ \epsilon_{22}^e \ \epsilon_{33}^e \ \epsilon_{23}^e \ \epsilon_{13}^e \ \epsilon_{12}^e]^T, \tag{66}$$

$$\bar{\sigma} = [\sigma_{11} \ \sigma_{22} \ \sigma_{33} \ \sigma_{23} \ \sigma_{13} \ \sigma_{12}]^T, \tag{67}$$

and

$$\mathbf{b} = [f_{,\bar{\sigma}_1} \ f_{,\bar{\sigma}_2} \ f_{,\bar{\sigma}_3} \ f_{,\bar{\sigma}_4} \ f_{,\bar{\sigma}_5} \ f_{,\bar{\sigma}_6}]^T. \tag{68}$$

Defining the residual vector as  $\mathbf{r}(\mathbf{x}^k)$  and the vector of unknowns as  $\mathbf{x}^k$ , we have

$$\mathbf{r}(\mathbf{x}^k) = \left\{ \begin{array}{l} \hat{\mathbf{x}} - \bar{\epsilon}_{n+1}^{e,tr} + \Delta\lambda \mathbf{b} \\ f(\sigma_{n+1}, p_{c,n+1}) \end{array} \right\}_{7 \times 1}^k, \quad \mathbf{x}^k = \left\{ \begin{array}{l} \bar{\epsilon}^e \\ \Delta\lambda \end{array} \right\}_{7 \times 1}^k,$$

where  $\hat{\mathbf{x}}$  is a vector containing the first six components of  $\mathbf{x}$ , and  $k$  is an iteration counter. The local tangent operator  $\mathbf{r}'(\mathbf{x}^k)$  is obtained from the following equation:

$$\mathbf{r}'(\mathbf{x}^k) = \left[ \begin{array}{c|c} \left( \Delta\lambda \frac{\partial \mathbf{b}}{\partial \hat{\mathbf{x}}} + \mathbf{I} \right)_{6 \times 6} & \mathbf{b}_{1 \times 6} \\ \hline \left( \mathbf{b}^T \mathbf{C}^e - \bar{\mathbf{a}}_T \bar{\sigma}_{n+1} \left( \frac{\partial p_{c,n+1}}{\partial \hat{\mathbf{x}}} \right)^T \right)_{1 \times 6} & 0_{1 \times 1} \end{array} \right]_{7 \times 7}^k, \tag{69}$$

where  $\mathbf{I}$  denotes a  $6 \times 6$  identity matrix, and

$$\frac{\partial \mathbf{b}}{\partial \hat{\mathbf{x}}} = \frac{\partial \mathbf{b}}{\partial \bar{\sigma}_{n+1}} \frac{\partial \bar{\sigma}_{n+1}}{\partial \hat{\mathbf{x}}} + \frac{\partial \mathbf{b}}{\partial p_{c,n+1}} \frac{\partial p_{c,n+1}}{\partial \hat{\mathbf{x}}} \tag{70}$$

$$= \frac{1}{M^2} \mathbf{A}_T \mathbf{C}^e + 2\bar{\mathbf{a}}_T^T \bar{\mathbf{a}}_T \mathbf{C}^e - \bar{\mathbf{a}}_T^T \frac{\partial p_{c,n+1}}{\partial \hat{\mathbf{x}}}. \tag{71}$$

The Newton–Raphson iteration for  $\mathbf{x}$  begins with initial estimates  $(\epsilon_{n+1}^e)^k = \epsilon_{n+1}^{e,tr}$  and  $\Delta\lambda^k = 0$  for iteration number  $k = 0$ .

Apart from the local tangent operator  $\mathbf{r}'(\mathbf{x})$ , a global tangent operator is also needed in order to obtain optimal convergence rate in the global Newton iteration within a stress-driven simulation. The algorithmic tangent operator is defined as

$$\mathbb{C}_{n+1} = \frac{\partial \sigma_{n+1}}{\partial \epsilon_{n+1}} = \frac{\partial \sigma_{n+1}}{\partial \epsilon_{n+1}^{e,tr}}. \tag{72}$$

Because the calculations presented in this section are to be carried out at load step  $n + 1$ , we herein drop the index  $n + 1$  for brevity. At the converged step of the local Newton iteration, the vector of unknowns has components

$$\mathbf{x} = [\epsilon_{11}^e \ \epsilon_{22}^e \ \epsilon_{33}^e \ \epsilon_{23}^e \ \epsilon_{13}^e \ \epsilon_{12}^e \ \Delta\lambda]^T. \tag{73}$$

Because  $\partial \sigma / \partial \epsilon^e = \mathbb{C}^e$ , a simple application of the chain rule gives

$$\mathbb{C} = \frac{\partial \sigma}{\partial \epsilon} = \mathbb{C}^e : \frac{\partial \epsilon^e}{\partial \epsilon}. \tag{74}$$

This suggests that we need to obtain the derivative  $\partial \epsilon^e / \partial \epsilon$ .

At the final step of local Newton iteration, we have  $\mathbf{r}(\mathbf{x}^*) = \mathbf{0}$ , where  $\mathbf{x}^*$  is the solution of the local problem. Therefore,

$$\frac{\partial \mathbf{r}}{\partial \epsilon} = \frac{\partial \mathbf{r}}{\partial \epsilon} \Big|_{\mathbf{x}} + \frac{\partial \mathbf{r}}{\partial \mathbf{x}} \Big|_{\epsilon^{e,tr}} \frac{\partial \mathbf{x}}{\partial \epsilon} = \mathbf{0}, \tag{75}$$

where it is understood that all  $\mathbf{x}$  variables are evaluated at  $\mathbf{x}^*$ . Solving,

$$\frac{\partial \mathbf{x}}{\partial \boldsymbol{\epsilon}} = -\mathcal{J}^{-1} \left. \frac{\partial \mathbf{r}}{\partial \boldsymbol{\epsilon}} \right|_{\mathbf{x}}, \tag{76}$$

where  $\mathcal{J}$  is the local tangent operator given in Equation (69) and evaluated at the converged step, and

$$\left. \frac{\partial \mathbf{r}}{\partial \boldsymbol{\epsilon}} \right|_{\mathbf{x}} = \begin{bmatrix} \left. \frac{\partial \mathbf{r}_{(1:6)}}{\partial \boldsymbol{\epsilon}^{e,tr}} \right|_{\mathbf{x}} : \frac{\partial \boldsymbol{\epsilon}^{e,tr}}{\partial \boldsymbol{\epsilon}} \\ \left. \frac{\partial f}{\partial \boldsymbol{\epsilon}} \right|_{\mathbf{x}} \end{bmatrix}_{7 \times 6}, \tag{77}$$

where  $\mathbf{r}_{(1:6)}$  denotes a vector containing the first six rows of  $\mathbf{r}$ . Further, we can write

$$\left. \frac{\partial f}{\partial \boldsymbol{\epsilon}} \right|_{\mathbf{x}} = -(\mathbf{a}^* : \boldsymbol{\sigma}) \left. \frac{\partial p_c}{\partial \boldsymbol{\epsilon}^{e,tr}} \right|_{\mathbf{x}}, \quad \frac{\partial \boldsymbol{\epsilon}^{e,tr}}{\partial \boldsymbol{\epsilon}} = \mathbb{I}, \tag{78}$$

in which

$$\left. \frac{\partial p_c}{\partial \boldsymbol{\epsilon}^{e,tr}} \right|_{\mathbf{x}} = \left( \frac{p_c}{\lambda^p} \right) \mathbf{1}. \tag{79}$$

$$\left. \frac{\partial^2 f}{\partial \boldsymbol{\sigma} \partial \boldsymbol{\epsilon}^{e,tr}} \right|_{\mathbf{x}} = -\mathbf{a}^* \otimes \left. \frac{\partial p_c}{\partial \boldsymbol{\epsilon}^{e,tr}} \right|_{\mathbf{x}} = -(p_c/\lambda^p) \mathbf{a}^* \otimes \mathbf{1}. \tag{80}$$

Finally, upon substituting (77)–(80) into (76), we obtain

$$\frac{\partial \mathbf{x}}{\partial \boldsymbol{\epsilon}} = -\mathcal{J}^{-1} \begin{bmatrix} -\mathbf{I}_{6 \times 6} - (p_c/\lambda^p) \Delta \lambda \boldsymbol{\mu} \\ -\vartheta \tilde{\mathbf{1}} \end{bmatrix}, \tag{81}$$

where  $\tilde{\mathbf{1}}$  is the Kronecker delta in vector form,  $\boldsymbol{\mu} = \bar{\mathbf{a}}_T^T \tilde{\mathbf{1}}$ , and  $\vartheta = -(p_c/\lambda^p) \mathbf{a}^* : \boldsymbol{\sigma}$ . The components of  $\partial \boldsymbol{\epsilon}^e / \partial \boldsymbol{\epsilon}$  can then be substituted into (74) to obtain the algorithmic tangent operator.

### 5. SHEAR BAND BIFURCATION

This section revisits the balance of energy, particularly Equation (20), for developing relevant criteria for shear band bifurcation in thermoelastoplastic solids. We consider two extreme cases: isothermal bifurcation and adiabatic bifurcation. Each of the two cases is described in the succeeding text.

#### 5.1. Isothermal localization

Isothermal localization occurs when heat conducts rapidly enough for the jump in temperature across a shear band to be negligible. This occurs, for example, when the heat conductivity  $\kappa$  is sufficiently high that all mechanically generated heat dissipates rapidly. In this case,  $\dot{\Theta}$  may be set to zero, and (60) reduces to

$$\dot{\boldsymbol{\sigma}} = \mathbb{C}^{ep} : \dot{\boldsymbol{\epsilon}}. \tag{82}$$

Now, consider a potential band with unit normal  $\mathbf{n} = n_i \mathbf{e}_i$ , as shown in Figure 3. The equilibrium condition on the band states that the traction rate outside the band must equal the traction rate inside the band, that is,

$$\mathbf{n} \cdot \dot{\boldsymbol{\sigma}} = \mathbf{n} \cdot \dot{\boldsymbol{\sigma}}', \tag{83}$$

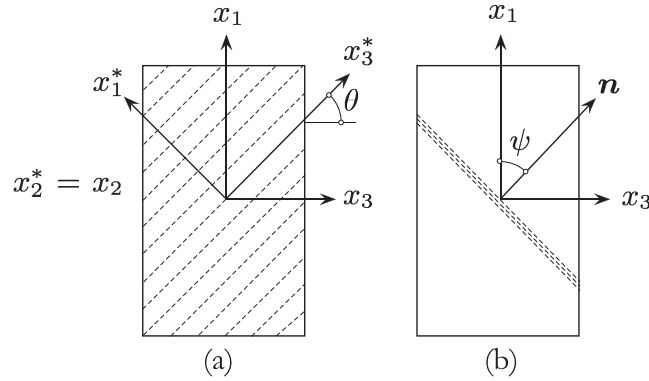


Figure 3. Schematic of (a) plane of isotropy and (b) deformation band. Notations:  $x_1^*$  is the axis of symmetry;  $\mathbf{n}$  is the normal to the shear band;  $\theta$  is the angle between planes of isotropy (bedding planes) and  $x_3$ ;  $\psi$  is the angle between normal to the shear band and  $x_1$ .

where  $\dot{\sigma}$  and  $\dot{\sigma}'$  are understood to be the Cauchy stress rates outside and inside the band, respectively.

For a loading/loading bifurcation mode [8], strains and stresses can be linked using the same continuum elastoplastic tangential moduli tensor  $\mathbb{C}^{ep}$ , as shown in Equation (82). Using indicial notation, we thus have

$$n_i \mathbb{C}_{ijk l}^{ep} \dot{\epsilon}_{kl} = n_i \mathbb{C}_{ijk l}^{ep} (\dot{\epsilon}_{kl} + \llbracket \tilde{v}_k \rrbracket n_l), \tag{84}$$

where  $\llbracket \tilde{v}_k \rrbracket = \llbracket v_k \rrbracket / h$  is the velocity jump inside the band, normalized with respect to shear band thickness  $h$ , which produces the additional strain rate  $\llbracket \tilde{v}_k \rrbracket n_l$  inside the band.

The equilibrium condition takes the form

$$A_{jk}^{ep} \llbracket \tilde{v}_k \rrbracket = 0, \quad A_{jk}^{ep} = n_i \mathbb{C}_{ijk l}^{ep} n_l. \tag{85}$$

The eigenvalue problem is then phrased as follows,

$$A^{ep} \cdot \mathbf{m} = \mathbf{0}, \quad A^{ep} = \mathbf{n} \cdot \mathbb{C}^{ep} \cdot \mathbf{n}, \tag{86}$$

where  $\mathbf{m}$  is a unit vector in the direction of  $\llbracket \tilde{\mathbf{v}} \rrbracket$ . The term  $A^{ep}$  is normally called the elastoplastic acoustic tensor in shear band analysis. Non-trivial solution leads to finding the stress state and shear band normal  $\mathbf{n}$  where the localization function vanishes for the first time, that is,

$$F = \min_{\mathbf{n}} \det(A^{ep}) = 0. \tag{87}$$

This is the classic shear band bifurcation problem for isothermal localization, which is well understood in the literature (e.g., [7, 8, 84]).

### 5.2. Adiabatic localization

Adiabatic localization generally applies to deformation at high strain rates where mechanically generated heat does not have enough time to flow. This occurs, for example, in the processing and machining of metals and polymers and in rapid deformation of rocks during earthquake fault slips [87]. In this case, due either to low heat conductivity of the material and/or to high rate of plastic deformations, the heat flux can be assumed to be zero. Conceptually, the process is analogous to undrained shear band bifurcation in porous media (e.g., [88]), where rapid deformation and/or low permeability of the material inhibits the flow of water through the pores of the solid matrix.

For purposes of adiabatic localization analysis, we assume that the heat source in Equation (20) is zero, that is,  $r_t = 0$ , and also set  $\mathbf{q} = \mathbf{0}$ . Thus, we obtain

$$\rho c \dot{\Theta} = \zeta \boldsymbol{\sigma} : \dot{\boldsymbol{\epsilon}}^p. \tag{88}$$

Using the additive split of strain rate shown in Equation (15), we can write

$$\dot{\Theta} = \frac{\zeta}{\rho c} \boldsymbol{\sigma} : (\dot{\boldsymbol{\epsilon}} - \dot{\boldsymbol{\epsilon}}^e - \dot{\boldsymbol{\epsilon}}^t) = \frac{\zeta}{\rho c} \boldsymbol{\sigma} : (\dot{\boldsymbol{\epsilon}} - \mathbb{S} : \dot{\boldsymbol{\sigma}} + \boldsymbol{\alpha}^t \dot{\Theta}) . \tag{89}$$

Rearranging the terms yields

$$\dot{\Theta} = \frac{\zeta}{\phi^t \rho c} (\boldsymbol{\sigma} : \dot{\boldsymbol{\epsilon}} - \boldsymbol{\sigma} : \mathbb{S} : \dot{\boldsymbol{\sigma}}) , \tag{90}$$

where

$$\phi^t = 1 - \frac{\zeta}{\rho c} \boldsymbol{\sigma} : \boldsymbol{\alpha}^t . \tag{91}$$

Substituting (90) into (60) and rearranging the terms once again yield

$$\mathbb{L}^{-1} : \dot{\boldsymbol{\sigma}} = \mathbb{B} : \dot{\boldsymbol{\epsilon}} , \tag{92}$$

where

$$\mathbb{L}^{-1} = \mathbb{I} + \frac{\zeta}{\phi^t \rho c} \boldsymbol{\tau} \otimes (\boldsymbol{\sigma} : \mathbb{S}) , \quad \mathbb{B} = \mathbb{C}^{ep} + \frac{\zeta}{\phi^t \rho c} \boldsymbol{\tau} \otimes \boldsymbol{\sigma} . \tag{93}$$

The result is the following thermoelastoplastic constitutive relationship:

$$\dot{\boldsymbol{\sigma}} = \mathbb{C}^{ept} : \dot{\boldsymbol{\epsilon}} , \quad \mathbb{C}^{ept} = \mathbb{L} : \mathbb{B} . \tag{94}$$

We shall call  $\mathbb{C}^{ept}$  as the continuum thermoelastoplastic tangential moduli tensor, which is analogous to the undrained tangential moduli tensor in hydro-mechanical problems [88].

For adiabatic localization, the onset of shear band bifurcation requires the solution of the eigenvalue problem

$$\mathbf{A}^{ept} \cdot \mathbf{m} = \mathbf{0} , \quad \mathbf{A}^{ept} = \mathbf{n} \cdot \mathbb{C}^{ept} \cdot \mathbf{n} , \tag{95}$$

which means finding the stress state and critical shear band normal  $\mathbf{n}$  at which the thermoelastoplastic acoustic tensor  $\mathbf{A}^{ept}$  becomes singular for the first time, that is,

$$\tilde{F} = \min_{\mathbf{n}} \det(\mathbf{A}^{ept}) = 0 . \tag{96}$$

The term  $\mathbf{A}^{ept}$  is analogous to the undrained acoustic tensor used in hydro-mechanical bifurcation analysis [88].

## 6. STRESS-POINT SIMULATIONS

Through numerical examples at the stress-point level, we illustrate the basic features of the proposed anisotropic thermoplasticity model in this section. We first consider triaxial compression test data available in the literature to calibrate the model from experiments and then demonstrate the capability of the model in capturing the anisotropic behavior of the material. Next, we carry out plane-strain simulations to study shear band localization in anisotropic materials, as well as to differentiate between isothermal and adiabatic localization.

### 6.1. Model calibration

The following simulations aim at demonstrating the performance of the proposed model in capturing experimental observations without thermal effects. For this purpose, we calibrated the present model using the experimental data obtained by Niandou *et al.* [83] for samples of Tournemire shale. In their paper, Niandou *et al.* present triaxial test results for three different orientations of bedding plane, at  $\theta = 0^\circ, 45^\circ,$  and  $90^\circ,$  and at different confining stresses. For purposes of simulation, we set initial stress values  $\sigma_{11} = \sigma_{22} = \sigma_{33} = \sigma_c$  and then increase the magnitude of the compressive stress  $\sigma_{11}$  while holding  $\sigma_{22}$  and  $\sigma_{33}$  fixed. The deviator stress is then defined as  $q = |\sigma_{11} - \sigma_{22}| = \sigma_{22} - \sigma_{11}$ . The reader is referred to Figure 3 for a schematic of the problem. Replacing  $\mathbf{a}^*$  in Equation (40) with

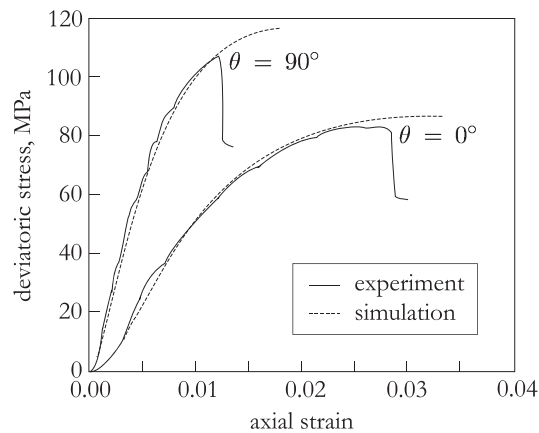


Figure 4. Comparison of model predictions and triaxial test data for Tournemire shale at a confining stress of  $\sigma_c = -30$  MPa. Experimental data after [83].

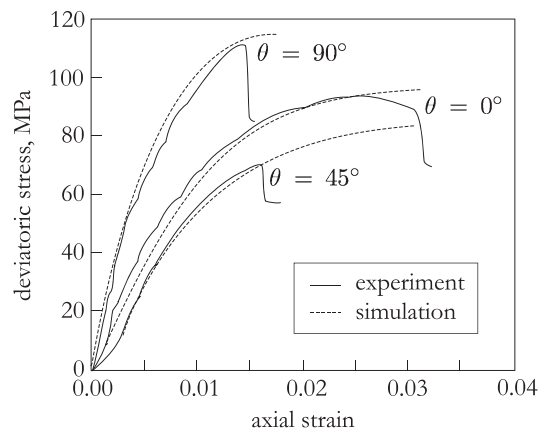


Figure 5. Comparison of model predictions and triaxial test data for Tournemire shale at a confining stress of  $\sigma_c = -40$  MPa. Experimental data after [83].

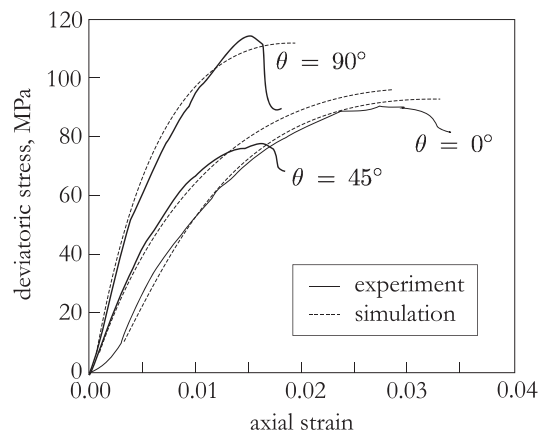


Figure 6. Comparison of model predictions and triaxial test data for Tournemire shale at a confining stress of  $\sigma_c = -50$  MPa. Experimental data after [83].

Table I. Plasticity parameters for Tournemire shale calibrated from triaxial compression tests.

$-\sigma_c$ [MPa]	$M$	$\alpha$	$\beta$
30	1.19	1.00	0.67
40	1.07	0.94	0.70
50	1.14	1.16	0.86

For all tests  $\gamma = 1$ .

$\mathbf{a}$ , while keeping  $\mathbb{A}^*$ , was observed to provide a better match with the experimental results, which suggests that anisotropy manifests itself in the deviatoric part of stress for this particular material. This has been taken into account in the numerical simulations presented in this paper.

Figures 4–6 show comparisons between the results of the present model simulations and experimental data for confining stresses  $\sigma_c = -30$ ,  $-40$ , and  $-50$  MPa (negative for compression), respectively. For  $\sigma_c = -30$  MPa, only the results for  $\theta = 0^\circ$  and  $\theta = 90^\circ$  are shown, as experimental data for  $\theta = 45^\circ$  were not reported in [83]. The hardening parameter is obtained as  $\lambda^p = 0.0026$ , while the rest of the parameters are reported in Table I. Note that the experiments were separately calibrated at each confining pressure to determine best-fit values. The resulting parameter values in Table I are fairly consistent across confining pressures, however, and in practice, a single (averaged) parameter set could be adopted.

It can be seen from these figures that the present model captures the overall plastic behavior and anisotropic nature of the samples quite well. These figures also show that for orientation of bedding plane other than  $\theta = 0^\circ$ , and under smaller values of confining stress, failure occurs during the hardening portion of stress–strain curve because of factors not taken into consideration in the stress–point simulations, such as delamination along the bedding planes, crack growth, and so on. As quantitative details of these heterogeneities have not been reported in [83], we assumed that the samples were all initially homogeneous.

Some final remarks are in order regarding the results of the aforementioned simulations. First, it is well known that initial heterogeneities do enhance failure, and thus, the laboratory samples failed before they could undergo large plastic deformations. Second, the experimental results shown in Figures 4–6 demonstrate a closure phase for the initial fractures at the beginning of axial loading, as discussed in [83]. This closure phase was not taken into account in the present simulations, as it is linked to initial cracks and fractures in lieu of the plastic behavior of the matrix itself. Thus, the simulation curves have been shifted slightly to the right where the experimental data suggested significant closure phase prior to conventional plastic behavior.

## 6.2. Isothermal and adiabatic strain localization

We now focus the simulations on the effect of temperature on shear band bifurcation. For this purpose, we present results of hypothetical plane strain simulations demonstrating thermoelastoplastic shear band bifurcation in anisotropic material. Referring to Figure 3 once again, we consider a plane–strain compression test in which the confining pressure  $\sigma_{33}$  is held constant, while the axial strain is incrementally increased by  $\Delta\epsilon_{11}$ , during which time,  $\epsilon_{22} = 0$  because of the constraint of plane strain. Although this is a stress–point simulation, it can be treated as a mixed boundary–value problem in which stresses are prescribed on some boundaries (natural boundary condition), while strains are prescribed on the remaining boundaries (essential boundary condition).

The following material parameters, which are similar to those for Tournemire shale, are assumed for this example: elasticity parameters (Appendix A) are assumed as  $E_1 = 20,000$  MPa,  $E_2 = 45,000$  MPa,  $\nu_{12} = 0.30$ , and  $\nu_{23} = 0.25$ . Mass density is selected as  $\rho = 2700$  kg/m<sup>3</sup>; normalized heat capacity parameter  $\bar{c}$  is introduced as  $\bar{c} = c/c_0 \times 10^3$ , in which  $c_0 = 703$  J/kg-K; thermal expansion coefficient is taken as  $\alpha^t = \alpha^t \mathbf{1}$ , with  $\alpha^t = 10^{-5}/^\circ\text{C}$ ; initial temperature is assumed as  $T_0 = 25^\circ\text{C}$ . The following plasticity parameters are also assumed:  $\lambda^p = 0.0051$ ,  $\alpha = 1.25$ ,  $\beta = 0.95$ ,  $\gamma = 1.1$ . These values are approximately the same as those obtained from the Tournemire shale calibration. Preconsolidation pressure is taken as  $p_c = 50$  MPa and confining pressure  $\sigma_c =$

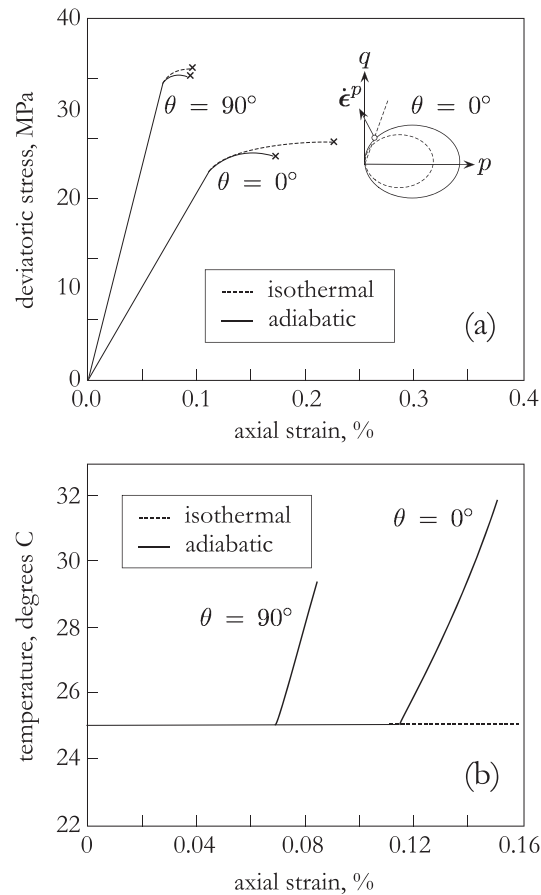


Figure 7. (a) Deviatoric stress versus axial strain response and (b) temperature profile for bedding plane orientations  $\theta = 0^\circ$  and  $90^\circ$ . Responses under isothermal conditions are compared with adiabatic response with normalized heat capacity parameter  $\bar{c} = 1$  and thermal softening coefficient  $\gamma_T = 0.261$ . Symbol  $\times$  denotes localization.

–1 MPa. The values for thermal softening parameter  $\gamma_T$  are selected to be consistent with the range of values calibrated by Laloui and Cekerevac [22]. In the numerical examples in this section,  $\Delta\epsilon_{11} = 10^{-5}$  has been used at each time step.

Figure 7(a) compares the deviatoric stress versus axial strain responses under isothermal and adiabatic conditions. Two different orientations of the bedding plane,  $\theta = 0^\circ$  and  $90^\circ$ , are considered. For the adiabatic case,  $\zeta = 1$ ,  $\gamma_T = 0.261$ , and  $\bar{c} = 1$  are used. Because the plastic strains in this particular example are small, smaller values of  $c$  were chosen to illustrate and study the thermal effects that can, in general, occur because of larger plastic deformations. The resultant temperature profile is shown in Figure 7(b), revealing the increase in temperature within the plastic range. It can be seen that even small changes in temperature (less than about  $10^\circ\text{C}$ ) impacts the plastic behavior and localization. Also, it can be seen that the sample for adiabatic simulation demonstrates a softer plastic behavior as a result of thermal softening. Consequently, bifurcation is detected at lower values of stress. Figures 8 and 9, on the other hand, demonstrate the influence of thermal softening parameter  $\gamma_T$  and specific heat on ensuing response. Resultant temperature profiles are also shown. It can be seen that higher values of  $\gamma_T$  and/or lower values of specific heat result in a softer material response, leading to larger plastic deformations. This causes a higher rate of increase in temperature, and, eventually, an earlier shear band bifurcation.

The insets shown in Figures 7–9 are various orientations of the yield surface on the  $p$ - $q$  plane for different bedding plane orientations  $\theta$  and are useful in the interpretation of the results. The stress paths considered in the simulations are denoted by the dashed straight lines emanating from

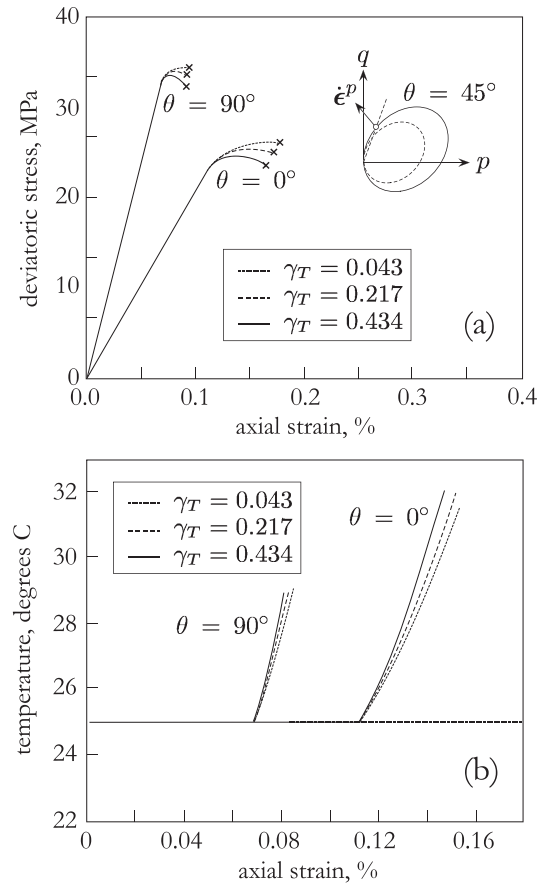


Figure 8. (a) Deviatoric stress versus axial strain response and (b) corresponding temperature profile for bedding plane orientations  $\theta = 0^\circ$  and  $90^\circ$ . Responses under adiabatic conditions with normalized heat capacity  $\bar{c} = 1$  are compared for different values of thermal softening coefficient  $\gamma_T$ . Symbol  $\times$  denotes localization.

the origin of the  $p$ - $q$  plane, all of which intersect the yield surface on the dilatant side, thus triggering strain softening at the moment of yielding (represented by the contracting ellipses). This explains why there is little plastic deformation needed to trigger strain localization. Because the flow rule considered is associative, the direction of the plastic strain increment  $\dot{\epsilon}^p$  has the greatest projection on the  $p$ -axis when the bedding plane is tilted away from either the horizontal or vertical axis, because in that case the yield surface is rotated in such a way as to favor the development of large plastic volumetric strain (Figure 8). This has important implications for the type of deformation band formed at the moment of bifurcation, as discussed further in the next section.

### 6.3. Dilation bands in anisotropic material

We now study the characteristics of localization under different orientations of planes of isotropy within the material. Bedding orientation is denoted herein by the angle  $\theta$ , which has the value zero with horizontal bedding and  $90^\circ$  with vertical bedding (Figure 3). For purposes of delineating shear band orientation, we define  $\psi$ , also shown in Figure 3, as the angle that the normal to the shear band makes with the vertical axis. Isotropic plasticity models typically yield two conjugate shear bands upon localization. However, in the present discussion, anisotropy leads to only one dominant shear band when the bedding plane is neither horizontal nor vertical. This result is consistent with experimental observations (e.g., [89]). To demonstrate this, Figure 10 shows determinant of elastoplastic acoustic tensor with an offset of  $10^2$  versus  $\psi$  for bedding plane orientations  $\theta = 0^\circ$ ,  $45^\circ$ , and  $90^\circ$ .

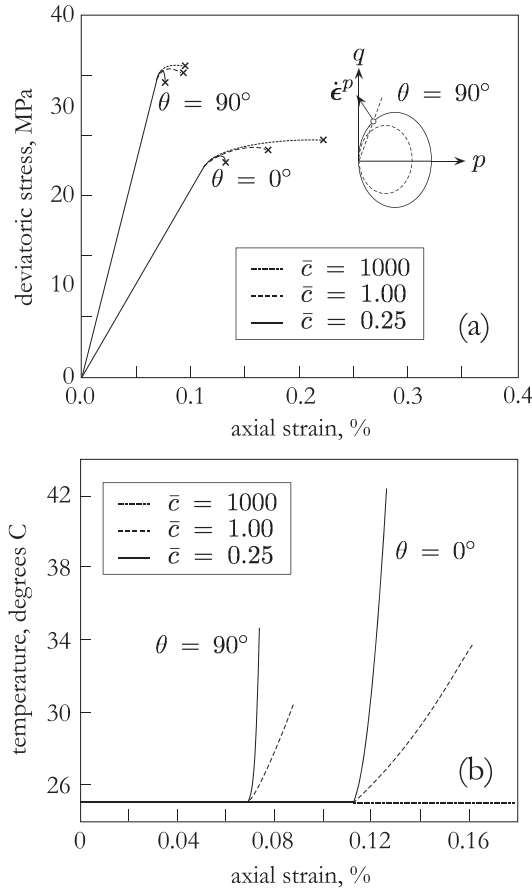


Figure 9. (a) Deviatoric stress versus axial strain response and (b) corresponding temperature profile for bedding plane orientations  $\theta = 0^\circ$  and  $90^\circ$ . Responses under adiabatic conditions with thermal softening coefficient  $\gamma_T = 0.217$  are compared for different values of normalized heat capacity parameter  $\bar{c}$ . Symbol  $\times$  denotes localization.

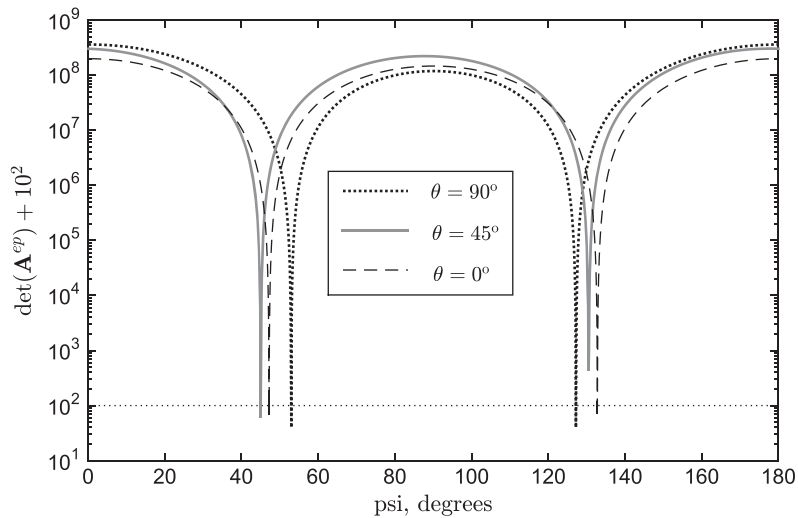


Figure 10. Determinant of elastoplastic acoustic tensor with an offset of  $10^2$  versus orientation of deformation band  $\psi$  for bedding plane orientations  $\theta = 0^\circ$ ,  $45^\circ$ , and  $90^\circ$ . Horizontal dashed line at  $10^2$  denotes bifurcation criterion.

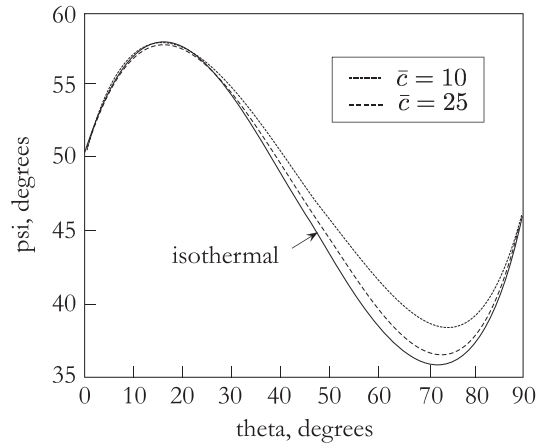


Figure 11. Orientation of deformation band ‘psi’ ( $= \psi$ ) as a function of orientation of bedding plane ‘theta’ ( $= \theta$ ).

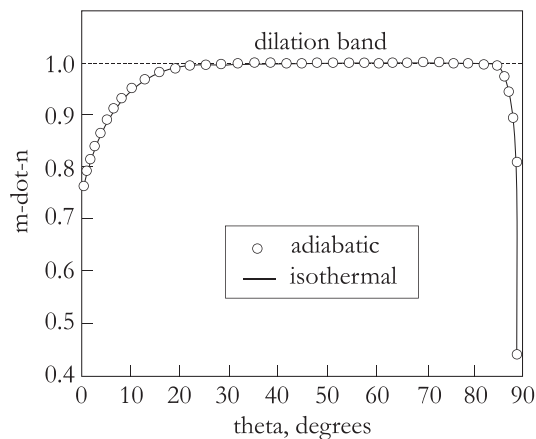


Figure 12. Plot of scalar product  $\mathbf{m} \cdot \mathbf{n}$  versus bedding plane orientation  $\theta$  showing anisotropy enhancing the formation of dilation band in plane strain compression.

It can be seen that for  $\theta = 0^\circ$  and  $90^\circ$ , two critical shear band orientations cross zero at the same time step. On the other hand, for  $\theta = 45^\circ$  one of the critical shear band orientations crosses zero first and forms the dominant shear band.

We assume the following parameters in the simulations:  $M = 1.45$ ,  $\lambda^p = 0.00065$ ,  $\alpha = 1.15$ ,  $\beta = 0.92$ ,  $\gamma = 1.1$ ,  $p_c = 50$  MPa,  $\sigma_c = -1$  MPa,  $\gamma_T = 0.261$ . The rest of the material parameters are the same as those reported in the previous section. Figure 11 shows the variation of  $\psi$  with  $\theta$  for isothermal and adiabatic localization. The curves shown in this figure are the loci of points at the instant when the determinant of the thermoelastoplastic acoustic tensor vanishes for the first time. For example, for isothermal localization with bedding plane at  $\theta \approx 73^\circ$ , the acoustic tensor becomes singular for the first time when the band orientation is at  $\psi \approx 35^\circ$ . Notice that deformation bands typically pass across the bedding planes in these simulations.

Classic bifurcation analysis also calculates the instantaneous direction of velocity jump from the eigenvector of the acoustic tensor, herein denoted by the unit vector  $\mathbf{m}$  [1, 2]. The scalar product  $\mathbf{m} \cdot \mathbf{n}$  thus defines the mode of the ensuing deformation band. Figure 12 plots the values of this scalar product for different bedding orientations  $\theta$  at the moment of bifurcation. Note from this figure that there is very little difference between the predicted types of deformation band, suggesting that the band does not depend on thermal conditions. This is to be contrasted with its hydromechanical counterpart, for which undrained bifurcation always forces the scalar product  $\mathbf{m} \cdot \mathbf{n}$  to have the value 0 because of the volume constraint induced by fluid flow [88]. In contrast, adiabatic localization

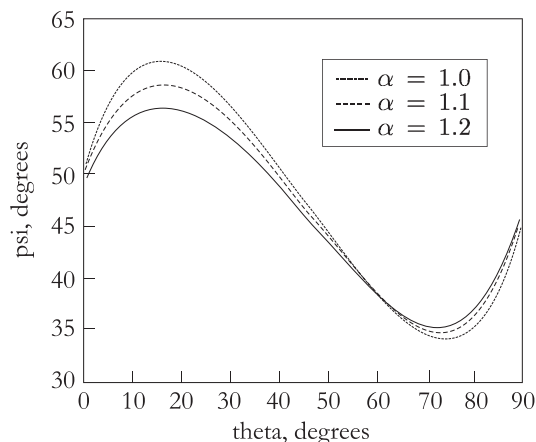


Figure 13. Influence of anisotropy parameter  $\alpha$  on the variation of band orientation  $\psi$  with respect to bedding plane orientation  $\theta$ .

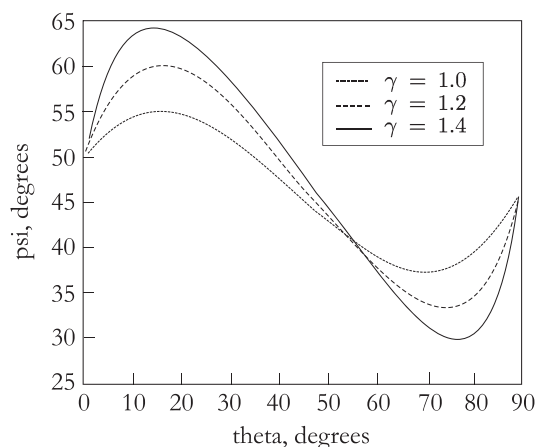


Figure 14. Influence of anisotropy parameter  $\gamma$  on the variation of band orientation  $\psi$  with respect to bedding plane orientation  $\theta$ .

does not involve a volume constraint, so there is little effect of thermal flow on the character of the ensuing deformation band.

Note that both adiabatic and isothermal simulations predict a significant range of possible bedding plane orientations at which a pure dilation band may be expected to emerge at bifurcation. As noted in the previous example, this is due to the fact that anisotropy rotates the yield surface in stress space in such a way as to favor the development of large plastic volumetric strain, as suggested in the inset of Figure 8. The normal to the yield surface in this case has significant component on the tension side of the  $p$ -axis, representing plastic dilation. Borja and Aydin [1] presented similar results for compaction bands, in which the normal to the yield surface has significant component on the compression side of the  $p$ -axis. Of course, this mode applies only to the moment of bifurcation; any process following that will reflect the evolution of the band at post-bifurcation.

Figures 13 and 14 show how the band orientation is influenced by the varying parameters  $\alpha$  and  $\gamma$ . Recall that these parameters determine the eventual orientation of the yield surface in  $p$ - $q$  space, and thus, have a direct bearing on ensuing deformation band. It can be seen that  $\alpha$  mostly affects the band orientation at smaller values of  $\theta$ . Because  $\gamma$  corresponds to shear terms, it does not affect the bifurcation angle at vertical or horizontal bedding plane orientations. However, it has the most impact on bedding plane orientations where shear stresses become

significant. Additional parametric studies (not shown) indicate that the  $m \cdot n$  versus  $\theta$  curves are not so much affected by the values selected for the parameters, suggesting that anisotropy does promote the formation of a dilation band.

7. SUMMARY AND CONCLUSIONS

We have presented an anisotropic thermoelastoplastic framework for modeling coupled thermo-mechanical behavior in transversely isotropic materials and for predicting the onset of strain localization in the form of a deformation band in these materials. The MCC model has been extended to account for anisotropy by introducing a microstructure tensor and a stress projection into a fictitious isotropic configuration. The model has been calibrated using experimental data for Tournemire shale. Anisotropy in the plastic behavior appears to depend mainly on the deviatoric component of stress for this particular material. The proposed model appears to capture the overall anisotropic mechanical behavior well. For low-confining pressures and/or non-horizontal bedding planes, however, microstructural heterogeneities in the form of microcracks could dominate the overall mechanical behavior. The proposed continuum model cannot handle these conditions, and more robust grain-scale models such as those developed in [90–93] are needed to capture such smaller-scale mechanisms.

Stress-point simulations of isothermal and adiabatic strain localization in anisotropic materials reveal one dominant shear band, in contrast to localization in isotropic materials where shear bands always appear in conjugate pair. An exception is when the bedding plane is either perpendicular or parallel to the major principal stress, in which case the effect of anisotropy is negated by the symmetric loading condition that gives rise to conjugate shear bands even in the presence of anisotropy. Under adiabatic conditions, samples generally demonstrate a softer behavior, and localization occurs at a lower stress level relative to isothermal condition. Increasing the thermal softening parameter and/or decreasing the heat capacity magnifies this trend. Adiabatic localization has a significant influence on the orientation of the deformation band. Finally, an interesting result of this study concerns the development of a pure dilation band. Anisotropy rotates the yield surface in such a way as to generate significant positive volumetric plastic strains, thus enhancing the development of a pure dilation band.

APPENDIX A: TRANSVERSELY ISOTROPIC LINEAR ELASTICITY

The stress–strain relationship for a linear elastic material can be written in matrix form as

$$\bar{\sigma} = [C^e] \bar{\epsilon}^e, \tag{A.1}$$

where  $\bar{\sigma} = [\sigma_{11} \ \sigma_{22} \ \sigma_{33} \ \sigma_{23} \ \sigma_{13} \ \sigma_{12}]^T$  and  $\bar{\epsilon}^e = [\epsilon_{11}^e \ \epsilon_{22}^e \ \epsilon_{33}^e \ \epsilon_{23}^e \ \epsilon_{13}^e \ \epsilon_{12}^e]^T$  are vector representations of the stress tensor and elastic strain tensor, respectively; and  $[C^e]$  is the linear elastic tangent represented in matrix form. The inverse of the elastic tangent (elastic compliance) can be written in the following matrix form for a transversely isotropic material:

$$[C^e]^{-1} = \begin{bmatrix} 1/E_1 & -\nu_{12}/E_2 & -\nu_{12}/E_2 & 0 & 0 & 0 \\ -\nu_{12}/E_2 & 1/E_2 & -\nu_{23}/E_2 & 0 & 0 & 0 \\ -\nu_{12}/E_2 & -\nu_{23}/E_2 & 1/E_2 & 0 & 0 & 0 \\ 0 & 0 & 0 & 0.5/G_{23} & 0 & 0 \\ 0 & 0 & 0 & 0 & 0.5/G_{12} & 0 \\ 0 & 0 & 0 & 0 & 0 & 0.5/G_{12} \end{bmatrix}. \tag{A.2}$$

Note that there are five independent elastic parameters, namely,  $E_1$ ,  $E_2$ ,  $\nu_{12}$ ,  $\nu_{23}$ , and  $G_{12}$ . The parameter  $G_{23}$  can be obtained using Young’s modulus in the isotropic plane as

$$G_{23} = \frac{E_2}{2(1 + \nu_{23})}, \tag{A.3}$$

while the parameter  $G_{12}$  can be determined by conducting tests where the major axes are not aligned with the bedding planes of the specimen. Alternatively,  $G_{12}$  can be approximated using Saint-Venant's formula [75] as

$$\frac{1}{G_{12}} = \frac{1}{E_1} + \frac{1}{E_2} + 2\frac{\nu_{12}}{E_1}. \quad (\text{A.4})$$

#### ACKNOWLEDGEMENTS

This material is based upon work supported by the U.S. Department of Energy, Office of Science, Office of Basic Energy Sciences, Chemical Sciences, Geosciences, and Biosciences Division, under award number DE-FG02-03ER15454. The first author acknowledges National Science Foundation Graduate Research Fellowship under grant no. DGE-114747. Portions of this work were performed by the first author on a summer internship at Lawrence Livermore National Laboratory, supported by the Stanford-Total Enhanced Modeling of Source Rock Project. LLNL is operated by Lawrence Livermore National Security, LLC, for the U.S. Department of Energy, National Nuclear Security Administration under contract DE-AC52-07NA27344.

#### REFERENCES

1. Borja RI, Aydin A. Computational modeling of deformation bands in granular media. I. Geological and mathematical framework. *Computer Methods in Applied Mechanics and Engineering* 2004; **193**(27–29):2667–2698.
2. Borja RI. Computational modeling of deformation bands in granular media. II. Numerical simulations. *Computer Methods in Applied Mechanics and Engineering* 2004; **193**(27–29):2699–2718.
3. Armero F, Garikipati K. An analysis of strong discontinuities in multiplicative finite strain plasticity and their relation with the numerical simulation of strain localization in solids. *International Journal of Solids and Structures* 1996; **33**(20):2863–2885.
4. Borja RI. Cam-clay plasticity. Part V: a mathematical framework for three-phase deformation and strain localization analyses of partially saturated porous media. *Computer Methods in Applied Mechanics and Engineering* 2004; **193**(48):5301–5338.
5. Hill R. A general theory of uniqueness and stability in elastic-plastic solids. *Journal of the Mechanics and Physics of Solids* 1958; **6**(3):236–249.
6. Regueiro RA, Foster CD, Borja RI, Fossum AF. *Bifurcation Analysis of a Three-invariant, Isotropic/kinematic Hardening Cap Plasticity Model for Geomaterials*. American Rock Mechanics Association: Houston, Texas, 2004.
7. Rice JR. *The Localization of Plastic Deformation*. Division of Engineering, Brown University: Providence, Rhode Island, 1976.
8. Rudnicki JW, Rice JR. Conditions for the localization of deformation in pressure-sensitive dilatant materials. *Journal of the Mechanics and Physics of Solids* 1975; **23**(6):371–394.
9. Śloderbach Z, Pajak J. The local conditions of uniqueness and plastic strain localization. Part I: determination of the critical hardening moduli for some elastoplastic materials. *Mathematics and Mechanics of Solids* 2011; **16**(1):18–35.
10. Śloderbach Z, Pajak J. The local conditions of uniqueness and plastic strain localization. Part II: comparison of the local uniqueness condition with the Rice–Rudnicki local plastic strain localization. *Mathematics and Mechanics of Solids* 2011; **16**(1):109–121.
11. Yuan Y, Xu B, Palmgren C. Design of caprock integrity in thermal stimulation of shallow oil-sands reservoirs. *Journal of Canadian Petroleum Technology* 2013; **52**(04):266–278.
12. Saliya K, Grgic D, Giot R, Giraud A. Thermo-hydro-mechanical modeling with Langmuir's adsorption isotherm of the CO<sub>2</sub> injection in coal. *International Journal for Numerical and Analytical Methods in Geomechanics* 2015; **39**(6):594–617.
13. White JA, Chiamonte L, Ezzedineb S, Foxalla W, Haoa Y, Ramirez A, McNaba W. Geomechanical behavior of the reservoir and caprock system at the In Salah CO<sub>2</sub> storage project. *Proceedings of the National Academy of Sciences*, Vol. 111(24), 2014; 8747–8752.
14. Di Donna A, Laloui L. Numerical analysis of the geotechnical behaviour of energy piles. *International Journal for Numerical and Analytical Methods in Geomechanics* 2015; **39**(8):861–888.
15. Dupray F, Laloui L, Kazangba A. Numerical analysis of seasonal heat storage in an energy pile foundation. *Computers and Geotechnics* 2014; **55**:67–77.
16. Erol S, François B. Thermal stresses in borehole heat exchangers. *International Journal for Numerical and Analytical Methods in Geomechanics* 2015; **39**(13):1450–1470.
17. Laloui L, Nuth M, Vulliet L. Experimental and numerical investigations of the behaviour of a heat exchanger pile. *International Journal for Numerical and Analytical Methods in Geomechanics* 2006; **30**(8):763–781.

18. Masri M, Sibai M, Shao JF. *Experimental Study of the Thermomechanical Behavior of the Petroleum Reservoir*. SPE Eastern Regional/AAPG Eastern Section Joint Meeting, Society of Petroleum Engineers: Pittsburgh, Pennsylvania, 2008.
19. Xu B, Yuan YG, Wang ZC. *Thermal Impact on Shale Deformation/Failure Behaviors—Laboratory Studies*. 45th US Rock Mechanics/Geomechanics Symposium. American Rock Mechanics Association: San Francisco, California, 2011.
20. Hueckel T, Baldi G. Thermoplasticity of saturated clays: experimental constitutive study. *Journal of Geotechnical Engineering* 1990; **116**(12):1778–1796.
21. François B, Laloui L. *Modelling the Thermo-plasticity of Unsaturated Soils, Constitutive Modeling of Geomaterials*. Springer: Berlin, Heidelberg, 2013.
22. Laloui L, Cekerevac C. Thermo-plasticity of clays: an isotropic yield mechanism. *Computers and Geotechnics* 2003; **30**(8):649–660.
23. Laloui L, François B. ACMEG-T: soil thermoplasticity model. *Journal of Engineering Mechanics* 2009; **135**(9):932–944.
24. Modaressi H, Laloui L. A thermo-viscoplastic constitutive model for clays. *International Journal for Numerical and Analytical Methods in Geomechanics* 1997; **21**(5):313–335.
25. Raude S, Laigle F, Giot R, Fernandes R. A unified thermoplastic/viscoplastic constitutive model for geomaterials. *Acta Geotechnica* 2015:1–21.
26. Zhou H, Hu D, Zhang F, Shao JF. A thermo-plastic/viscoplastic damage model for geomaterials. *Acta Mechanica Solida Sinica* 2011; **24**(3):195–208.
27. Cui YJ, Sultan N, Delage P. A thermomechanical model for saturated clays. *Canadian Geotechnical Journal* 2000; **37**(3):607–620.
28. Graham J, Tanaka N, Crilly T, Alfaro M. Modified Cam–Clay modelling of temperature effects in clays. *Canadian Geotechnical Journal* 2001; **38**(3):608–621.
29. Hueckel T, Borsetto M. Thermoplasticity of saturated soils and shales: constitutive equations. *Journal of Geotechnical Engineering* 1990; **116**(12):1765–1777.
30. Mróz Z, Raniecki B. On the uniqueness problem in coupled thermoplasticity. *International Journal of Engineering Science* 1976; **14**(2):211–221.
31. Robinet JC, Rahbaoui A, Plas F, Lebon P. A constitutive thermomechanical model for saturated clays. *Engineering Geology* 1996; **41**(1):145–169.
32. Raniecki B, Sawczuk A. Thermal effects in plasticity. Part I: Coupled theory. *ZAMM - Journal of Applied Mathematics and Mechanics/Zeitschrift für Angewandte Mathematik und Mechanik* 1975; **55**(6):333–341.
33. Simo JC, Miehe C. Associative coupled thermoplasticity at finite strains: formulation, numerical analysis and implementation. *Computer Methods in Applied Mechanics and Engineering* 1992; **98**(1):41–104.
34. Armero F, Simo JC. A priori stability estimates and unconditionally stable product formula algorithms for nonlinear coupled thermoplasticity. *International Journal of Plasticity* 1993; **9**(6):749–782.
35. Mróz Z, Raniecki B. A derivation of the uniqueness conditions in coupled thermoplasticity. *International Journal of Engineering Science* 1976; **14**(4):395–401.
36. Raniecki B, Sawczuk A. Thermal effects in plasticity. Part II: uniqueness and applications. *ZAMM - Journal of Applied Mathematics and Mechanics/Zeitschrift für Angewandte Mathematik und Mechanik* 1975; **55**(7–8):363–373.
37. Śloderbach Z, Pająk J. Generalized coupled thermoplasticity taking into account large strains. Part I. conditions of uniqueness of the solution of boundary-value problem and bifurcation criteria. *Mathematics and Mechanics of Solids* 2010; **15**(3):308–327.
38. Swallowe GM. *Adiabatic Shear Bands in Polymers*. Adiabatic Shear Localization: Frontiers and Advances: Elsevier, Massachusetts, 2012.
39. Hartley KA, Duffy J, Hawley RH. Measurement of the temperature profile during shear band formation in steels deforming at high strain rates. *Journal of the Mechanics and Physics of Solids* 1987; **35**(3):283–301.
40. Marchand A, Duffy JS. An experimental study of the formation process of adiabatic shear bands in a structural steel. *Journal of the Mechanics and Physics of Solids* 1988; **36**(3):251–283.
41. Brun JP, Cobbold PR. Strain heating and thermal softening in continental shear zones: a review. *Journal of Structural Geology* 1980; **2**(1):149–158.
42. Poirier JP, Bouchez JL, Jonas JJ. A dynamic model for aseismic ductile shear zones. *Earth and Planetary Science Letters* 1979; **43**(3):441–453.
43. Poirier JP. Shear localization and shear instability in materials in the ductile field. *Journal of Structural Geology* 1980; **2**(1):135–142.
44. Sulem J. *Shear Localization in Deep Geological Layers During Seismic Slip*. Adiabatic Shear Localization: Frontiers and Advances: Elsevier, Massachusetts, 2012.
45. Bai YL. Thermo-plastic instability in simple shear. *Journal of the Mechanics and Physics of Solids* 1982; **30**(4):195–207.
46. Batra RC. Effect of material parameters on the initiation and growth of adiabatic shear bands. *International Journal of Solids and Structures* 1987; **23**(10):1435–1446.
47. Clifton RJ, Duffy J, Hartley KA, Shawki TG. On critical conditions for shear band formation at high strain rates. *Scripta Metallurgica* 1984; **18**(5):443–448.
48. Molinari A, Clifton RJ. Analytical characterization of shear localization in thermoviscoplastic materials. *Journal of Applied Mechanics* 1987; **54**(4):806–812.

49. Wright TW, Batra RC. The initiation and growth of adiabatic shear bands. *International Journal of Plasticity* 1985; **1**(3):205–212.
50. Benallal A, Bigoni D. Effects of temperature and thermo-mechanical couplings on material instabilities and strain localization of inelastic materials. *Journal of the Mechanics and Physics of Solids* 2004; **52**(3):725–753.
51. Duszek MK, Perzyna P. The localization of plastic deformation in thermoplastic solids. *International Journal of Solids and Structures* 1991; **27**(11):1419–1443.
52. Duszek MK, Perzyna P, Stein E. Adiabatic shear band localization in elastic-plastic damaged solids. *International Journal of Plasticity* 1992; **8**(4):361–384.
53. Duszek-Perzyna MK, Perzyna P. Analysis of anisotropy and plastic spin effects on localization phenomena. *Archive of Applied Mechanics* 1998; **68**(5):352–374.
54. Perzyna P. Instability phenomena and adiabatic shear band localization in thermoplastic flow processes. *Acta Mechanica* 1994; **106**(3-4):173–205.
55. Runesson K, Steinmann P, Larsson R. On localization in thermo-elastoplastic solids subjected to adiabatic conditions. *European Journal of Mechanics-A/Solids* 1999; **18**(4):557–579.
56. Armero F, Park J. An analysis of strain localization in a shear layer under thermally coupled dynamic conditions. Part 1: continuum thermoplastic models. *International Journal for Numerical Methods in Engineering* 2003; **56**(14):2069–2100.
57. Armero F, Park J. An analysis of strain localization in a shear layer under thermally coupled dynamic conditions. Part 2: localized thermoplastic models. *International Journal for Numerical Methods in Engineering* 2003; **56**(14):2101–2133.
58. LeMonds J, Needleman A. Finite element analyses of shear localization in rate and temperature dependent solids. *Mechanics of Materials* 1986; **5**(4):339–361.
59. Ngo VM, Ibrahimbegović A, Brancherie D. Model for localized failure with thermo-plastic coupling: theoretical formulation and ED-FEM implementation. *Computers and Structures* 2013; **127**:2–18.
60. Sanavia L, Pesavento F, Schrefler BA. Finite element analysis of non-isothermal multiphase geomaterials with application to strain localization simulation. *Computational Mechanics* 2006; **37**(4):331–348.
61. Bennett KC, Berla AL, Nix WD, Borja RI. Instrumented nanoindentation and 3D mechanistic modeling of a shale at multiple scales. *Acta Geotechnica* 2015; **10**(1):1–14.
62. McLamore R, Gray KE. The mechanical behavior of anisotropic sedimentary rocks. *Journal of Manufacturing Science and Engineering* 1967; **89**(1):62–73.
63. Nasser MHB, Rao KS, Ramamurthy T. Anisotropic strength and deformational behavior of Himalayan schists. *International Journal of Rock Mechanics and Mining Sciences* 2003; **40**(1):3–23.
64. Heuze FE. High-temperature mechanical, physical and thermal properties of granitic rocks—a review. *International Journal of Rock Mechanics and Mining Sciences and Geomechanics Abstracts* 1983; **20**(1):3–10.
65. Hill R. *The Mathematical Theory of Plasticity*. The Oxford Engineering Science Series: Oxford, 1950.
66. Hill R. A theory of the yielding and plastic flow of anisotropic metals. *Proceedings of the Royal Society of London. Series A. Mathematical and Physical Sciences* 1948; **193**(1033):281–297.
67. Hashagen F, de Borst R. Enhancement of the Hoffman yield criterion with an anisotropic hardening model. *Computers and Structures* 2001; **79**(6):637–651.
68. Hoffman O. The brittle strength of orthotropic materials. *Journal of Composite Materials* 1967; **1**(2):200–206.
69. Schellekens JCJ, de Borst R. The use of the Hoffman yield criterion in finite element analysis of anisotropic composites. *Computers and Structures* 1990; **37**(6):1087–1096.
70. Tsai SW, Wu EM. A general theory of strength for anisotropic materials. *Journal of Composite Materials* 1971; **5**(1):58–80.
71. Pariseau WG. Plasticity theory for anisotropic rocks and soil. *The 10th US Symposium on Rock Mechanics (USRMS)*, American Rock Mechanics Association, Austin, Texas, 1968.
72. Reinicke KM, Ralston TD. Plastic limit analysis with an anisotropic, parabolic yield function. *International Journal of Rock Mechanics and Mining Sciences and Geomechanics Abstracts* 1977; **14**(13):147–162.
73. Boehler JP, Sawczuk A. Equilibre limite des sols anisotropes. *Journal Mécanique* 1970; **9**:5–33.
74. Cazacu O, Cristescu ND, Shao JF, Henry JP. A new anisotropic failure criterion for transversely isotropic solids. *Mechanics of Cohesive-frictional Materials* 1998; **3**(1):89–103.
75. Crook AJL, Yu JG, Willson SM. *Development of an Orthotropic 3D Elastoplastic Material Model for Shale*. Society of Petroleum Engineers: Irving, Texas, 2002.
76. Nova R. The failure of transversely isotropic rocks in triaxial compression. *International Journal of Rock Mechanics and Mining Sciences and Geomechanics Abstracts* 1980; **17**(6):325–332.
77. Cazacu O, Cristescu ND. A paraboloid failure surface for transversely isotropic materials. *Mechanics of Materials* 1999; **31**(6):381–393.
78. Boehler JP, Sawczuk A. On yielding of oriented solids. *Acta Mechanica* 1977; **27**(1-4):185–204.
79. Chen L, Shao JF, Huang HW. Coupled elastoplastic damage modeling of anisotropic rocks. *Computers and Geotechnics* 2010; **37**(1):187–194.
80. Oka F, Kimoto S, Kobayashi H, Adachi T. Anisotropic behavior of soft sedimentary rock and a constitutive model. *Soils and Foundations* 2002; **42**(2):59–70.
81. Pietruszczak S, Lydzba D, Shao JF. Modelling of inherent anisotropy in sedimentary rocks. *International Journal of Solids and Structures* 2002; **39**(3):637–648.

82. Pietruszczak S, Mróz Z. Formulation of anisotropic failure criteria incorporating a microstructure tensor. *Computers and Geotechnics* 2000; **26**(2):105–112.
83. Niandou H, Shao JF, Henry JP, Fourmaintraux D. Laboratory investigation of the mechanical behaviour of Tournemire shale. *International Journal of Rock Mechanics and Mining Sciences* 1997; **34**(1):3–16.
84. Borja RI. *Plasticity Modeling and Computation*. Springer: Berlin, Heidelberg, 2013.
85. LeMonds J, Needleman A. An analysis of shear band development incorporating heat conduction. *Mechanics of Materials* 1986; **5**(4):363–373.
86. Picard JM. Ecroissage thermique des argiles saturées: application au stockage des déchets radioactifs. *PhD thesis*, Ecole nationale des ponts et chaussées-ENPC PARIS/MARNE LA VALLEE, 1994.
87. Dodd B, Bai Y. *Adiabatic Shear Localization: Frontiers and Advances*. Elsevier: Massachusetts, 2012.
88. Borja RI. Condition for liquefaction instability in fluid-saturated granular soils. *Acta Geotechnica* 2006; **1**(4):211–224.
89. Tien YM, Kuo MC, Juang CH. An experimental investigation of the failure mechanism of simulated transversely isotropic rocks. *International Journal of Rock Mechanics and Mining Sciences* 2006; **43**(8):1163–1181.
90. Borja RI, Rahmani H. Computational aspects of elasto-plastic deformation in polycrystalline solids soils. *Journal of Applied Mechanics* 2012; **79**(3):031024.
91. Borja RI, Rahmani H. Discrete micromechanics of elastoplastic crystals in the finite deformation range. *Computer Methods in Applied Mechanics and Engineering* 2014; **275**:234–263.
92. Tjioe M, Borja RI. On the pore-scale mechanisms leading to brittle and ductile deformation behavior of crystalline rocks. *International Journal for Numerical and Analytical Methods in Geomechanics* 2015; **39**(11):1165–1187.
93. Tjioe M, Borja RI. Pore-scale modeling of deformation and shear band bifurcation in porous crystalline rocks. *International Journal for Numerical Methods in Engineering* 2016. DOI: 10.1002/nme.5208.